J. Fluid Mech. (2012), *vol.* 696, *pp.* 5–44.
doi:10.1017/jfm.2011.418

Bursting bubble aerosols

H. Lhuissier[1] **and E. Villermaux**[1,2]†

[1] Aix-Marseille Université, IRPHE, 13384 Marseille CEDEX 13, France
[2] Institut Universitaire de France, 75005 Paris, France

(Received 7 June 2011; revised 12 September 2011; accepted 22 September 2011;
first published online 18 November 2011)

We depict and analyse the complete evolution of an air bubble formed in a water bulk, from the time it emerges at the liquid surface, up to its fragmentation into dispersed drops. To this end, experiments describing the drainage of the bubble cap film, its puncture and the resulting bursting dynamics determining the aerosol formation are conducted on tapwater bubbles. We discover that the mechanism of *marginal pinching* at the bubble foot and associated convection motions in the bubble cap, known as *marginal regeneration*, both drive the bubble cap drainage rate, and are responsible for its puncture. The resulting original film thickness h evolution law in time, supplemented with considerations about the nucleation of holes piercing the film together culminate in a determination of the cap film thickness at bursting $h_b \propto R^2/\mathscr{L}$, where R is the bubble cap radius of curvature, and $\mathscr{L}$ a length which we determine. Subsequent to a hole nucleation event, the cap bursting dynamics conditions the resulting spray. The latter depends both on the bubble shape prescribed by R/a, where a is the capillary length based on gravity, and on h_b. The mean drop size $\langle d\rangle \sim R^{3/8}\, h_b^{5/8}$, the number of drops generated per bubble $N \sim (R/a)^2\,(R/h_b)^{7/8}$ and the drop size distribution $P(d)$ are derived, comparing well with measurements. Combined with known bubble production rates over the ocean, our findings offer an adjustable parameter-free prediction for the aerosol flux and spray structure caused by bubble bursting in this precise context.

Key words: aerosols/atomization, bubble dynamics, drops and bubbles

1. Introduction

The question of the aerosol flux from the Earth's surface to the atmosphere has been addressed since the work of Aitken (1881) on condensation nuclei. Among different production mechanisms, those occurring at the sea surface are predominant (Coantic 1980; Andreas *et al.* 1995; O'Dowd & de Leeuw 2007), in particular those associated with wave breaking at the coasts in the so-called 'surf zone'. The water surface agitation there induces various atomization processes (see e.g. figure 1), which also contribute to the sea/atmosphere water vapour exchanges, and global equilibrium at the Earth scale (Monahan & Dam 2001). For instance, sea spray evaporation is estimated to exceed natural evaporation once the wind speed exceeds 15 m s^{-1} (Latham & Smith 1990; Andreas *et al.* 1995).

† Email address for correspondence: villermaux@irphe.univ-mrs.fr

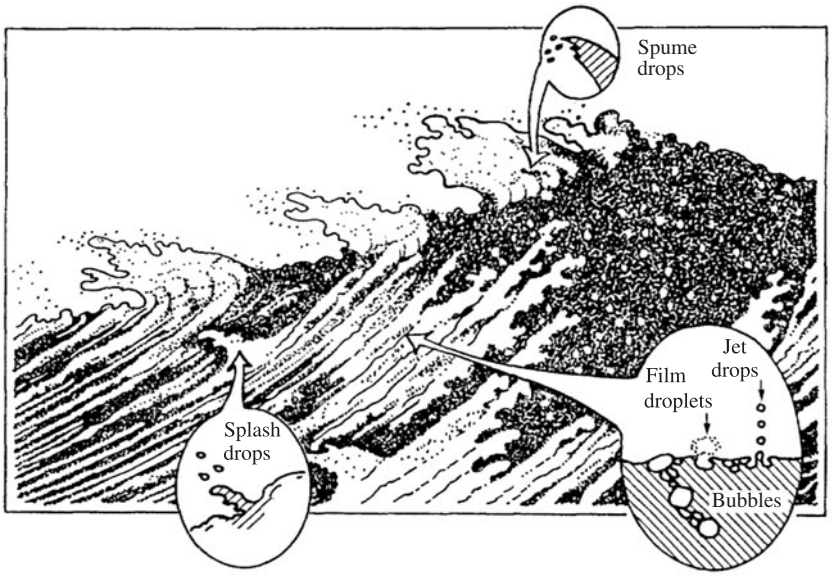

FIGURE 1. Origins of the different kinds of sea spray droplets. The present study concerns the 'film droplets' production mechanism. Adapted from figure 1 on page 5 of Andreas *et al.* (1995).

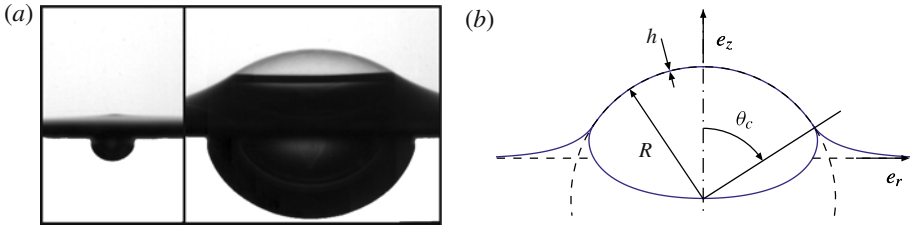

FIGURE 2. (*a*) Two bubbles of different sizes at the surface of a water bulk ($R \simeq 0.25$ and 3 mm respectively). (*b*) Schematic section of a millimetric bubble. The bubble cap is a film of thickness h, extending on a sphere portion of radius R and half-angle θ_c and connected to the bulk via the meniscus surrounding it.

Wave breaking produces a foam of bubbles, which eventually burst, projecting a large collection of drops into the air. Two processes are involved depending on the particular shape an air bubble adopts when it lies at the surface of a liquid bulk, as schematized in figure 2. A first fragmentation process was identified by Jacobs (1937) in the pinch-off of the well-known Worthington upward jet (Worthington & Cole 1897) formed from the collapse of the cavity by the sudden pressure drop following the bubble cap breakup. It concerns small bubbles, down to microns in size, and never produces more than ten 'jet drops' per bubble (Blanchard 1963). A second process, much more efficient and concerning millimetric bubbles was later identified by Knelman, Dombrowski & Newitt (1954). It consists of the disintegration of the thin liquid film separating the cavity from the atmosphere, the bubble cap, which produces up to hundreds of 'film drops' per bubble (Blanchard & Sysdek 1988; Resch & Afeti 1991; Spiel 1998).

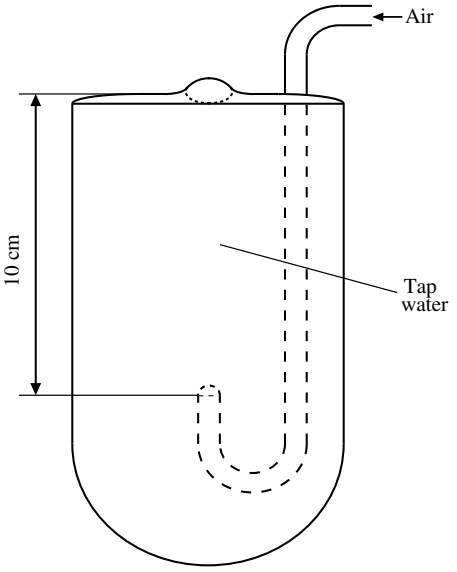

FIGURE 3. Bubbles are generated by injecting pressurized air into a bent pipe. Different bubbles sizes are obtained by changing the pipe outlet diameter and the air flow rate.

This paper is concerned with this latter mechanism. It aims to quantitatively estimate the inherent aerosol production by studying all the intermediate steps contributing to it. Our approach is to study isolated bubbles of cap radius R ranging from 100 μm to 1 cm, those corresponding to the film drop production range (see § 4) at the surface of a tapwater bulk. Their behaviour is found to be very similar to that of bubbles formed out of sea water (by contrast with soap bubbles where the presence of a large quantity of surfactant drastically alters the behaviour). Every step of the bubble life essential to understanding the cap disintegration is studied. We found no need to describe the precise bubble initiation below the liquid surface since the subsequent bubble evolution remained unchanged despite profound variations of formation mechanisms and depth of initiation (see the experimental set-up we finally adopted in figure 3).

Bubbles burst by nucleating a hole in their cap. The bursting dynamics depends, however, directly on the cap thickness h_b at the moment the hole forms; § 2 describes the bubble cap drainage and puncture. We observe that this problem can be split into two parts: a deterministic film thinning due to the liquid drainage into its base meniscus, and a hole nucleation event through the bubble cap which is stochastic and is analysed accordingly.

Liquid film drainage has already been intensively studied for foams and their broad applications. However the cap shape configuration of surface bubbles which imposes a pressure $2\sigma/R$ in the liquid of the film is not always accounted for (σ stands for the liquid surface tension). Even more important, most studies (Schwartz & Roy 1999; Howell 1999; de Gennes 2001; Aradian, Raphaël & de Gennes 2001; Breward & Howell 2002) use two-dimensional configurations implicitly assuming a symmetry of revolution, or horizontal translation invariance. They certainly offer a good description for soap films where large surface viscosities induced by large surfactant concentrations rapidly damp all motion in the film plane, but they cannot describe the drainage dynamics relevant for water bubbles where convection motions play a first-order role, as we will show. The marginal pinching occurring at the bubble

foot where the cap connects to its meniscus is indeed known to be unstable for low surface viscosity (Bruinsma 1995). The resulting convection cell emission is called *marginal regeneration* after Mysels, Shinoda & Frankel (1959). We develop in § 2.2 a heuristic model where all those features are articulated together, providing a thickness evolution law h agreeing quantitatively with the measurements.

The cap puncture mechanism is then considered. Puncture consists of nucleating a large enough hole through the cap, an event requiring an activation energy σh^2. It is shown that for the range of thickness $h_b \sim 100$ nm–10 μm involved, neither thermal fluctuations, nor marginal-regeneration-induced film turbulence can account for the puncture. The detailed puncture mechanism remains unclear; we nevertheless develop a model in § 3 based on the observation that puncture preferentially appears at the bubble foot within the convection cells, which accounts for the very robust observation that the cap mean thickness h_b at the onset of bursting scales as

$$h_b \simeq \frac{R^2}{\mathscr{L}} \tag{1.1}$$

as indicated by the measurements made by Spiel (1998) with seawater, and ours. We give an interpretation of the mysterious length $\mathscr{L}$.

The last step involved in the aerosol production is the cap disintegration. Although its dynamics is fast, typically less than 1 ms, unambiguous direct visualization using modern imagery (Photron APX) makes its study comparatively easier than that of drainage or puncture. Note however that neat observations do not require such elaborate apparatus: as early as in 1672, Robert Hooke noted that (citation reported by Plateau 1873)

> 'It is singular also that after that, when the bubble bursts, its rupture takes place with a species of explosion, by dispersing its parts in a kind of dust or fog'.

Later, Marangoni & Stefanelli (1872) even managed to see liquid ligaments, mediating the fragmentation into drops, by simply carefully watching a bursting bubble lit by a spark. Finally, perennial visual evidence of the breakup scenario has been available since the early age of cinematography from the stereoscopic movies by Etienne Jules Marey (Bull 1904), depicting unambiguously the whole sequence of the bursting of a soap bubble pierced by a bullet. In the context of marine aerosol production however, these precious observations seem to have been overlooked. As already mentioned, the group of Dombrowski identified the film disintegration as a droplet source (Newitt, Dombrowski & Knelman 1954), but together with Blanchard & Sysdek (1988), misunderstood its dynamics. The formation of ligaments actually results from the inertial destabilization of the rim bordering the opening hole, collecting the film liquid, as we show (see also Lhuissier & Villermaux 2009). Resch & Afeti (1991) obtained photographic evidence of this scenario but did not identify it and focused on drop size distributions without explaining their origin. Spiel (1998) was the first to propose a quantitative description of the average drop size. But although he noticed that the rim undergoes a centripetal acceleration as it recedes, he did not identified the Rayleigh–Taylor destabilization as the selection mechanism. He predicted that the angle covered by recession on the bubble cap before drop ejection occurs is independent of bubble size, in contradiction with our observations and understanding of them, which in addition provide good predictions for destabilization time, size of ligaments, number of droplets and droplets size distributions (§ 4).

In § 5, the results obtained on single bubbles are applied to the context of marine aerosols. *In situ* bubble population measurements by Deane & Stokes (2002) are used to estimate the net aerosol content due to film bubble disintegration. The corresponding prediction is seen to compare well with field measurements by Wu *et al.* (1984).

2. Drainage

A gas bubble at an interface can be schematically considered as a thin curved liquid film, the cap, connected to the bulk via a meniscus and enclosing an air cavity (see figure 2). In the same way, its lifetime can be seen as a relatively long, but variable period when the cap bubble thins as the cavity is immobile, inevitably ended by cap puncture. In this section we consider these successive steps. They result from the impossibility of a static equilibrium, leading to the liquid film drainage into the bulk.

2.1. *Bubble shape*

The bubble shape directly influences the film drainage through both the film orientation with respect to the direction of gravity, and capillary pressure induced by the interface curvatures. It also determines the bursting dynamics via the cap extension and curvature. The determination of this shape is thus mandatory for understanding the whole bubble lifetime and it is our starting point.

The bubble shape is prescribed by the size of the bubble, say its cap radius of curvature R, relative to the capillary length $a = \sqrt{\sigma/\rho g}$, which determines whether capillarity σ/R dominates gravity $\rho g R$, where ρ is the liquid density. The shape can be determined by assuming hydrostatic equilibrium in the bulk and in the meniscus and obeying the Young–Laplace equation at each interface. As will be seen in § 2.2.1, the film thickness h is nearly instantaneously small enough for its weight to be neglected. In the same way, relative surface tension variations $\Delta\sigma/\sigma$, which are mandatory for sustaining the bubble, are small enough for surface tension to be considered as uniform. The weightless bubble cap thus adopts a hemispherical shape whose extension is imposed by the air cavity volume and the conditions at the meniscus. Figure 4 shows numerical bubble profiles obtained for bubbles of different relative sizes R/a with the same approach as Toba (1959) (see appendix A). As one would expect, small bubbles are found to be almost spherical and totally immersed in the liquid whereas large ones float and adopt a hemispherical shape.

For $R < a$, the relative cap extension varies strongly with R. In the limit case $R \ll a$, gravity plays no role and the bubble cavity is expected to be spherical and maintained below the surface. Pressure jumps at the interfaces impose the cavity radius to be half the cap radius R, because the cap is a film and has two interfaces while the cavity has a single one. The resultant buoyancy

$$\rho g \frac{4\pi}{3}\left(\frac{R}{2}\right)^3 \tag{2.1}$$

is therefore equilibrated by the surface tension vertical component $\sigma \sin\theta_c$ applied on the cap perimeter

$$\sigma \sin\theta_c \times 2\pi R \sin\theta_c \tag{2.2}$$

where θ_c is the half-cap-angle defining its extension, as sketched in figure 2. Thus θ_c is written

$$\lim_{R/a\to 0} \theta_c = \frac{R}{2\sqrt{3}a}. \tag{2.3}$$

Figure 4(*b*) shows that this approximation is valid up to surprisingly large bubble radii, namely as large as $R = 5a$. This is precisely the range of bubble sizes we will be

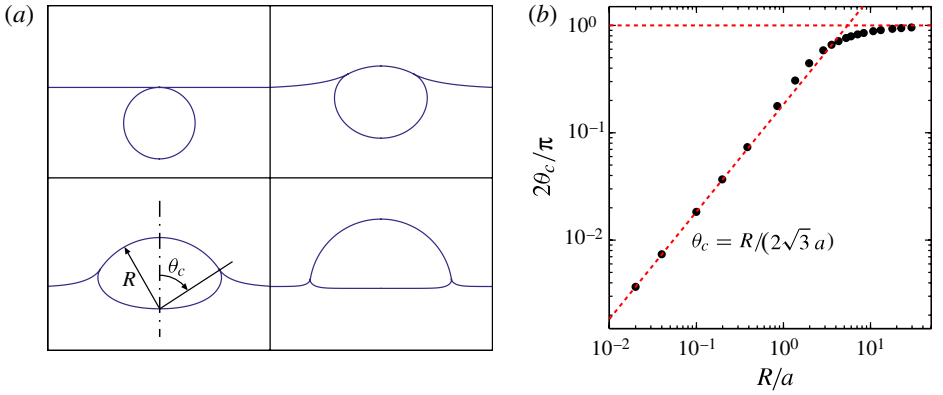

FIGURE 4. (Colour online available at journals.cambridge.org/flm) (*a*) Bubble shapes for increasing radii R (not to scale). (*b*) Cap angle θ_c versus bubble radius R (•) obtained by numerical integration of the Young–Laplace equation using *Mathematica* software (see appendix A). Dashed lines (−−) show asymptotic behaviours defined in (2.3).

concerned with (see § 4). Therefore, in the following, if not otherwise mentioned, the cap half-extension $E = R\theta_c$ will be considered to be of order

$$E = R\theta_c \sim \frac{R^2}{a}. \tag{2.4}$$

2.2. *Cap film drainage*

When an air bubble arrives from the bulk at the surface of water, the liquid layer separating it from the atmosphere emerges above the surface level to form the cap. It then necessarily drains into the bulk. The driving effect of this drainage flow is either the capillary pressure inside the cap $2\sigma/R$, or the hydrostatic pressure ρgR depending on the ratio R/a as discussed above. For the range of sizes $R \leqslant 5a$ that we are concerned with, the capillary pressure is always comparable to, or dominates, hydrostatic pressure. If the bubble exists at the surface for more than a fraction of a second, gravity imposes that a vertical surface tension gradient is established to sustain the liquid, and this is permitted by a concentration gradient of surfactants (unavoidably present in tap- or seawater) along the bubble cap. Three successive stages can then be distinguished (at least conceptually): a primary fast inertial drainage when the flow in a film section is typically a plug flow, a subsequent drainage when the surfactant monolayer stretches on the bubble cap and concentrates at its foot until the necessary surface tension gradient is established (§ 2.2.1), and a last slow drainage which involves both viscous and convection flows (§ 2.2.2).

2.2.1. *Fast early drainage and surfactants*

Initial free drainage begins during the emergence of the air cavity above the bulk and proceeds until the surface tension gradient required to balance the cap liquid weight is established. Most of the cap initial liquid is evacuated back to the bulk within this stage which typically lasts a capillary emptying time (remember capillary pressure dominates hydrostatic pressure) $\sqrt{\rho RE^2/\sigma}$, where ρ is the liquid density. For $R = a \simeq 2.7$ mm in water, this time is of order 10^{-2} s and decreases strongly with R. The remaining thickness at the end of this fast early drainage depends strongly on water purity.

If water is pure, the liquid in the film is free to slip at the interface and drains in a plug flow. The only slowing effect thus potentially resides in the film viscous

stretching but its characteristic time $\eta R/\sigma \sim 10^{-4}$ s, where η is the liquid viscosity, makes it ineffective even for centimetric water bubbles (note that this time scale corresponds to the drainage time $\eta/\rho g R$ observed by Debrégeas, de Gennes & Brochard-Wyart (1998) for 'bare' molten glass bubbles when gravity is the driving force). Such pure water bubbles thus drain and burst almost immediately after reaching the surface. This peculiar behaviour has been noticed by Newitt *et al.* (1954) and precisely accounted for by Blanchard, Bilofsky & Bridgman (1972). It was also observed in our experiments.

On the other hand, for the usual case of non-distilled water, bubbles can exist for a time t longer than 1 s, as suggested by common observation with tapwater or any kind of water found in nature – in rivers, oceans or rain puddles. The fundamental idea is that this latter behaviour is by far the more common, either in nature or in man-made processes, since an astonishingly small amount of surface-active components is required to maintain the bubble integrity. Actually we were able to obtain lasting bubbles in distilled water exposed for only a few seconds to the laboratory atmosphere. The particularly high surface energy of water is thus crucial for the bubble lifetime via its strong propensity to adsorb pollutants at its interface, a fact known long ago (Hagen 1846). We are specifically concerned with bubbles formed out of such highly diluted solutions. They represent an intermediary state between immediately bursting pure liquid bubbles, and saturated soap bubbles lasting minutes or hours, which are completely different both regarding their drainage dynamics, and puncture mechanism (see § 3).

We thus consider bubbles whose liquid films are sandwiched between two *mobile* monolayers of surfactants at each interface. In this condition, drainage remains free as long as the momentum diffusion time across a film section h^2/ν is short compared to the capillary emptying time $\sqrt{\rho R E^2/\sigma}$. Equating the two characteristic times yields the magnitude of the thickness h_η at which the monolayers start to be stretched by the interstitial flow:

$$h_\eta \sim \left(\frac{\eta^2 a^3}{\rho\sigma}\right)^{1/4}\left(\frac{R}{a}\right)^{5/4} \sim 10\text{–}100\ \mu\text{m}. \tag{2.5}$$

This is not necessarily the film thickness at the beginning of the viscous drainage that we will discuss in § 2.2.2; surface tension gradients of the surface monolayers are also to be considered.

Surface tension variations result from inhomogeneities in the surface concentration c of impurities adsorbed at the interface. In the dilute limit we are considering, the surface spreading pressure isotherm reduces to

$$\sigma_0 - \sigma = k_B T c \tag{2.6}$$

where σ_0 is the surface concentration of the pure solution, k_B is the Boltzmann constant and T is temperature. Impurities which are initially evenly distributed at the water interface are dragged down during the transition between the inertial and the viscous state by the downward film flow over the bubble cap. This effect is illustrated in figure 5 where the liquid surface has been seeded with micrometric bubbles acting roughly as passive surface tracers which are expelled radially as the bubble emerges, leaving a 'clean' interface over the bubble cap.

The bubble apex surface concentration is thus lowered by the surface stretching, concomitant with the film thinning, until the surface tension difference $\Delta\sigma$ (between the bubble apex and the bulk) required to maintain equilibrium is established. That difference is the sum of two contributions. The first one, corresponding to the film

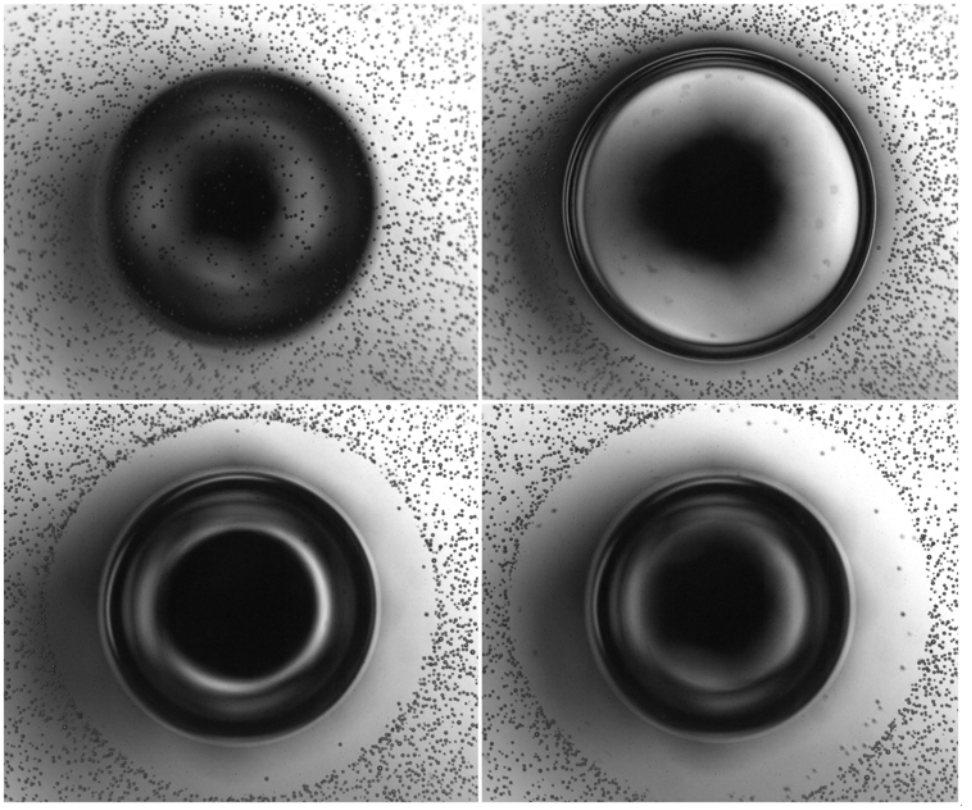

FIGURE 5. Cleaning of the interface accompanying the emergence of an air bubble at the bulk surface seen from above. The interface was previously seeded with homogeneously spread small bubbles of diameters between 10 and 50 μm. The bubble cap radius is $R \simeq 5$ mm, and time between images is 14 ms.

liquid weight projection along the local film tangent direction, is $\rho ghR(1-\cos\theta_c)/\sigma \leqslant Rh/a^2$. The second one, which is due to the shear stresses across the pinching region that form at the bubble foot (described in § 2.2.3), is of order $\sigma h/R$ leading to

$$\frac{\Delta\sigma}{\sigma} \sim \frac{Rh}{a^2} + \frac{h}{R}. \tag{2.7}$$

The thickness at the beginning of the viscous drainage can therefore be estimated if the initial spreading pressure $\sigma_0 - \sigma_b$ is known, where σ_b is the bulk surface tension, since it represents an upper bound for surface tension difference $\Delta\sigma$ between any pair of points at the liquid interface. Expressing that the film further thins by stretching the surface monolayers until $\Delta\sigma$ adapts to this maximal value, we have from (2.7) and (2.6) a new expression for the thickness at the end of the free-fall drainage regime:

$$h_\sigma \sim a\frac{\sigma_0 - \sigma_b}{\sigma_0}\left(\frac{a}{R} + \frac{R}{a}\right)^{-1}. \tag{2.8}$$

In all our experiments on bubble drainage and lifetime, we used the 'same' tapwater for the bulk solution. Its surface tension at 20 °C was measured by the pendant drop method yielding $\sigma_b = 71.2$ mN m^{-1} with a relative standard deviation of 0.6 % over 16

drops. Comparison with tabulated values for pure water $\sigma_0 = 72.7 \pm 0.05$ mN m^{-1} (Lide 1999) gives an estimate of $\sigma_0 - \sigma_b \sim 1$ mN m$^{-1} \ll \sigma_0$.

This shows that for the bubbles we are concerned with, the limiting condition for the thickness at the end of the free-fall drainage regime is $h = h_\sigma \ll h_\eta$. These values for $\sigma_0 - \sigma_b$ and h_σ also justify the assumptions made in § 2.1, namely that surface tension is essentially uniform and that the cap liquid weight is negligible.

These values for σ_b also show that the surface properties of our tapwater are very close to those of seawater. Indeed, although it is somewhat larger due to the presence of dissolved salt, the surface tension of seawater is well known to be of the same order as that of pure water (and thus of the same order as that of tapwater). Blanchard (1963), p. 117, for instance mentions for North Atlantic seawater at 22 °C a value of 73.2 mN m^{-1}. The corresponding capillary lengths can thus safely be considered as essentially equal numerically.

For the more subtle question of the surface pressure which plays the first-order role in the drainage dynamics, it also seems that tapwater can be considered as a very good experimental model for seawater. The presence of surface-active components in seawater is indeed ascertained (Jarvis *et al.* 1967). Moreover, its surface pressure seems to depend only very weakly on the specific sea under consideration and has a robust value of the order of 1 mN m^{-1} (Barger, Daniel & Garrett 1974).

These considerations justify that tapwater is a good experimental model for seawater and that the conclusion drawn from our experiments may safely be extended to the bubbles at the surface of the oceans.

2.2.2. *Viscous drainage*

Once the surface tension gradient supporting the cap liquid weight is set, the drainage of the cap consists of two opposite fluxes. Interstitial liquid is flowing downward to the bulk while surface components are being pushed upward as the liquid weight to bear decreases. The extrapolated final state, in the absence of puncture, is a vanishingly thin film covered by a uniform surface concentration.

The rate of drainage is not determined by the flow over the whole bubble cap but is instead prescribed by the conditions at the foot of the bubble, where the cap connects to the meniscus. Indeed, immediately after the formation of a bubble, a two-dimensional convection motion develops over the cap. This motion, which is generic to liquid films connected to a bulk or a frame, is called *marginal regeneration* following Mysels *et al.* (1959)'s description of the phenomenon. It consists of the periodic emission of regularly spaced plumes which form at the lower edge of the cap, where it connects to the meniscus. Figure 6 shows a sequence of this phenomenon observed on a flat water film connected to a bulk. It is evidenced by the interferences fringes revealing iso-thickness lines. Once they have left the pinching zone, the thinner plumes rise due to their positive buoyancy with respect to the surrounding thicker portions of the film.

For convenience, marginal regeneration observations were mainly carried out at the base of flat films since lighting and imaging are easier. However, it takes place in exactly the same way on hemispherical bubbles as can be clearly seen on figure 7 or figure 17. These two figures illustrate that the convection cells invade the whole cap surface and thus cause an efficient two-dimensional turbulent mixing over the whole liquid film. This leads to a very uniform thickness h of the film over all the cap as suggested by the constancy of the opening Taylor–Culick velocity $V = \sqrt{2\sigma/\rho h}$ (Taylor 1959; Culick 1960) of a hole growing in the cap (see § 4).

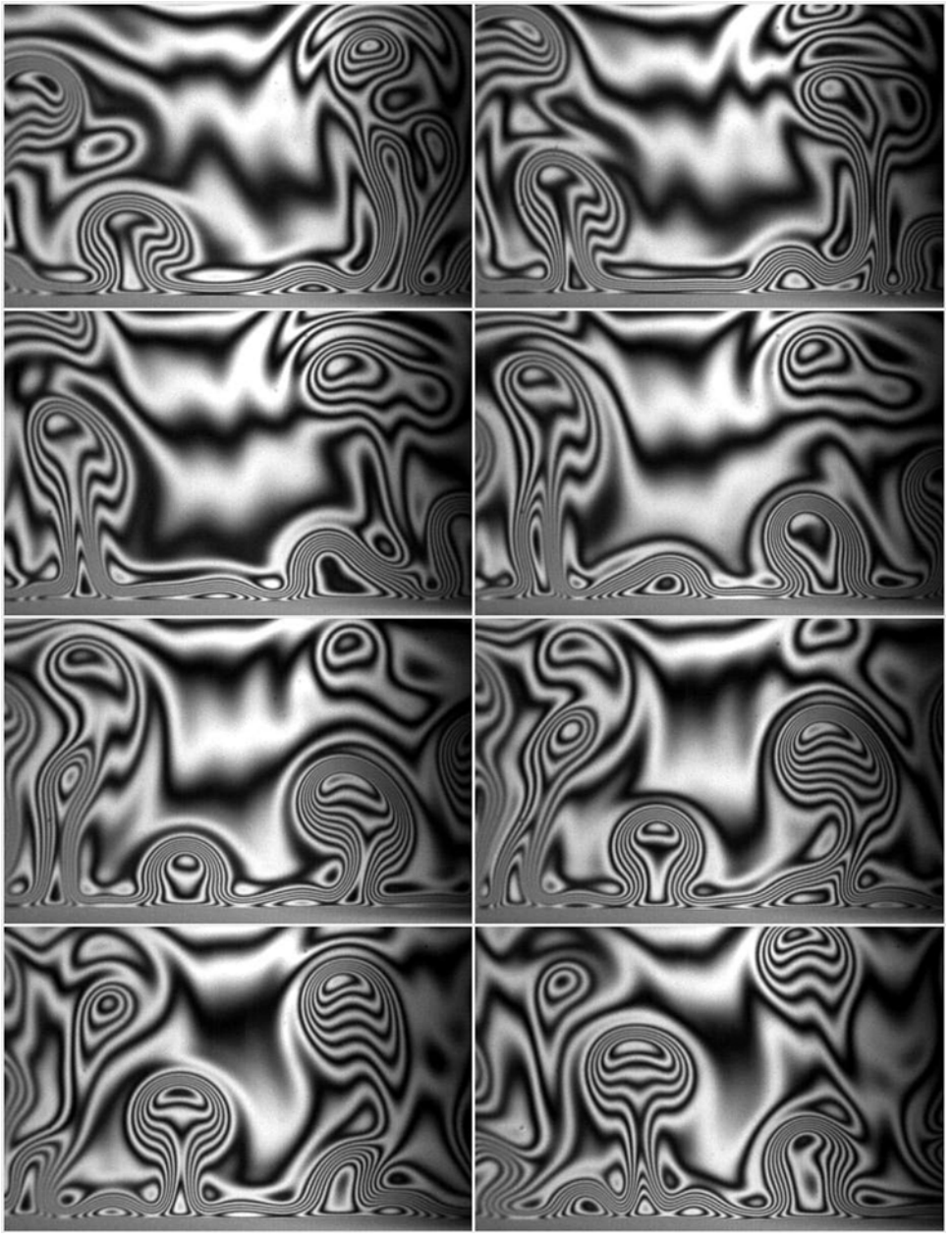

FIGURE 6. Marginal regeneration resulting from the pinch-off line instability at the bottom of a flat water film connected to a bulk (time increase from top left to bottom right). Fringes are iso-thickness lines obtained under monochromatic lighting (sodium lamp at 589 nm). The meniscus is the blurred band at the bottom of each picture. It is separated from the film by a line of minimal thickness (along a vertical direction): the *pinch-off* line. Thin convection cells develop by contorting the upper border of the pinch-off region. They then rise and separate from the meniscus (see the typical velocity field they generate in figure 14). Image width is 4.3 mm and time between images is 5/100 s.

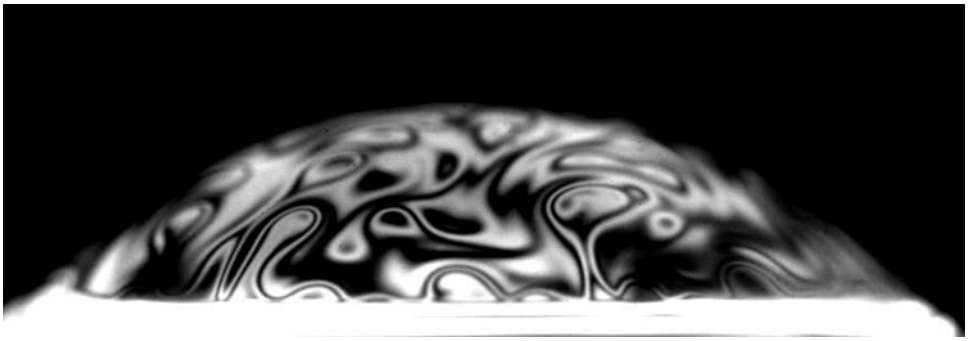

FIGURE 7. View of the convections plumes and of the overall turbulent mixing under monochromatic lighting (sodium lamp at 589 nm). Fringes are film iso-thickness lines. The very bright portion at the bottom of the picture is the meniscus. Bubble radius is $R = 5$ mm.

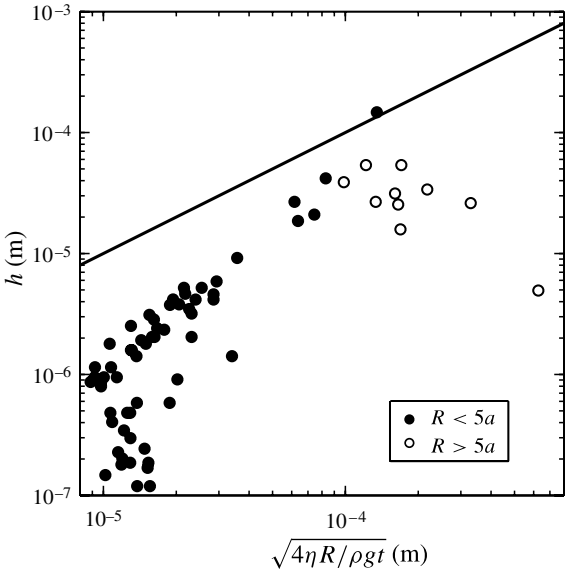

FIGURE 8. Comparison of the (*inappropriate*) drainage law (2.9) with experiments.

The mean film thickness h decreases as the film drains but does so more rapidly than would be expected from a cap Poiseuille-flow-limited thinning. The pressure within the cap $2\sigma/R$ is indeed uniform and in that context the viscous flow would be driven by gravity only, leading to a cap thickness evolution law

$$h = F(\theta)\sqrt{\frac{4\,\eta}{\rho g R\, t}}, \tag{2.9}$$

where $F(\theta)$ is a function that does not depend on the cap extension θ_c and is almost uniform between $F(\theta = 0) = 1$ and $F(\theta = \pi/2) \simeq 0.76$ (see appendix B). The law (2.9) relies on the assumption, obviously contradicted by the present observations, that the cap thickness follows the axial symmetry of revolution of the bubble

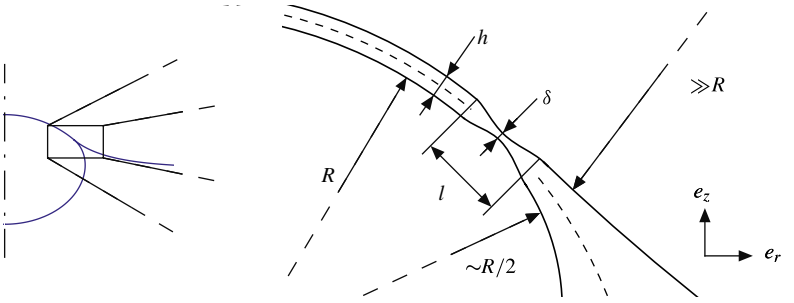

FIGURE 9. Sketch of the pinching region.

and, not surprisingly, it differs from the experimental measurements by strongly underestimating the drainage rate of small bubbles of extension $R\theta_c \ll R$ (see figure 8). This suggests that drainage is, rather, driven by convection motions and capillary pressure $2\sigma/R$.

2.2.3. *Pinching and marginal regeneration*

The standard Poiseuille-flow-limited thinning being not appropriate, we look for an alternative mechanism, and focus on the conditions at the foot of the bubble, where the film connects to the meniscus. The pressure within the liquid film is the capillary pressure $p = 2\sigma/R$ due to the cap curvature, where we have chosen the atmospheric pressure $p_a = 0$ as the reference pressure. At the meniscus, on the other hand, the hydrostatic pressure is recovered, with magnitude very small by comparison with p, and for the sake of clarity we will neglect it in the following (this pressure is $-\rho g z_m$, where z_m is the height of the top of the meniscus above the horizontal surface level, and its magnitude $\rho g z_m$ is always small compared to $p - p_a$).

The pressure difference between the film and the meniscus generates a flow from the former to the latter. This flow leads to the formation of a localized pinching separating the two regions, as described in Aradian *et al.* (2001). This pinching is clearly seen in figures 6 and 15, and is depicted in the sketch of figure 9. The pinched region of the film is typically described by its length l and its minimal thickness δ at the neck. Equilibrium requires that the curvature of the interfaces evolves in accordance with the pressure drop accompanying the inner viscous flow. The order of magnitude of l and δ can be determined by assuming that the axial symmetry of the bubble does not modify singularly the mechanism of the pinching, as experiments suggest. We will therefore only consider the interface curvature in the $(\boldsymbol{e_r}, \boldsymbol{e_z})$-plane. The pinching shape is prescribed by the viscous flow across it. It connects the cap where thickness and pressure are uniform because of the strong agitation, with the meniscus where viscous effects are negligible because it is thick, and where hydrostatic equilibrium prevails. Viscous dissipation is localized at the pinching and the flow of characteristic velocity u there thus induces a pressure loss $2\sigma/R$ over its length l:

$$\frac{\eta u}{\delta^2} \sim \frac{\sigma}{R\,l}. \tag{2.10}$$

This pressure drop is accompanied by a regular surface curvature increase ensuring the surface equilibrium condition. The matching of the pinching surface curvature with

that of the bubble cap R imposes

$$\frac{h-\delta}{l^2} \sim \frac{1}{R} \tag{2.11}$$

and we finally obtain

$$Ca \sim \frac{\delta^2}{R^{3/2}\,(h-\delta)^{1/2}} \sim \frac{\delta^2}{R^{3/2}h^{1/2}} \tag{2.12}$$

where $Ca = \eta u/\sigma$ is a capillary number. As long as nothing disturbs the pinching, it is expected to thin further as $\delta \propto t^{-1/2}$, being concentrated in an ever shorter length $l \propto t^{-1/4}$, due to the relaxation of the adjacent film portion (see Aradian *et al.* 2001). However, this predicted evolution may be actually seen on 'rigid' films only where the surfactant monolayers confer a 'solid' behaviour to the cap, and prevent any destabilization of the pinching region.

On the contrary, in the more common case of a 'liquid' or mobile monolayer, as for the present experiments, the marginal regeneration phenomenon resulting from the destabilization of the pinching line is rapidly observed. This destabilization, of a Bénard–Marangoni type, is driven by the surface tension difference across the pinching region (see § 2.3). This difference, of order

$$\Delta\sigma = \frac{2\delta}{R}\sigma \tag{2.13}$$

where $2\sigma/R$ is the pressure difference between the bubble cap and the meniscus base, is a consequence of the tangential viscous stresses pulling the surfactant monolayers towards the bulk. The larger the surface tension difference, the higher the propensity to level it by convection motions. We therefore assume that at any moment, marginal regeneration regulates the pinching thickness, with value corresponding to the critical onset of the pinching destabilization, and that it remains always of the order the film thickness, i.e.

$$\delta \lesssim h. \tag{2.14}$$

This crucial assumption agrees well with our experiments with tapwater and for which the following observations were systematically made:

(*a*) the pinching forms within a hundredth of a second after the emergence of the bubble;

(*b*) it lasts for the whole bubble lifetime;

(*c*) as seen in figures 6 and 15, it is continuously destabilized by convection cells, consisting of thinner film portions (and presumably of smaller surface tension) growing within the pinching region and then rising over the bubble cap;

(*d*) the pinching neck thickness δ is, from counting interference fringes, never smaller than half the film thickness h.

This last observation, paraphrasing (2.14), is also consistent with Mysels *et al.* (1959)'s remark (p. 35) that relative thickness differences are below 10 % and more recently with experiments by Nierstrasz & Frens (1998) (with low-concentration solutions of SDS and on a range of film thicknesses from 300 to 1500 nm) where a constant thickness ratio of approximatively 0.8 between the recently formed rising film portions (coming from the pinching region), and the rest of the film was systematically found.

The thickness of the bubble cap is uniform and its drainage is thus entirely determined by the liquid flux across the pinching line. This flux, from the cap to the meniscus, is the sum of the contributions of two mechanisms operating concomitantly:

(*a*) the direct flow across the pinching zone with rate prescribed by viscous stresses through the film thickness;

(*b*) the convective flow resulting from marginal regeneration motions along the cap surface tangent direction, with net flow rate achieved by cyclically replacing thick film portions by thinner ones.

The two mechanisms above are coupled. The liquid flux due to the convection motion is slaved to that due to the direct flow and is always of the same order of magnitude, an assumption leading to a good description of the experimental results over the whole range of bubbles $R \leqslant 5a$ we have investigated.

With these considerations in mind, assumption (2.14) and the scaling laws (2.10), (2.11) and (2.12), we have

$$l \sim \sqrt{R\,h} \tag{2.15}$$

and are now able to determine the drainage velocity

$$u = \frac{\sigma}{\eta}\left(\frac{h}{R}\right)^{3/2} \tag{2.16}$$

and from it the thinning law of a bubble. Mass conservation implies

$$\dot{h} \sim -hu\frac{P}{S} \simeq -hu\frac{2}{R\theta_c} \sim -\frac{\sigma a}{\eta}\frac{h^{5/2}}{R^{7/2}} \tag{2.17}$$

where the perimeter P refers to that at the foot of the bubble and the surface S to that of the cap, their ratio being equal to $2/R\theta_c$ within a few percent for any angle $0 \leqslant \theta_c \leqslant \pi/2$. Integration of (2.17) yields the expected thinning law

$$h \sim a\left(\frac{\eta a}{\sigma t}\right)^{2/3}\left(\frac{R}{a}\right)^{7/3}. \tag{2.18}$$

It is compared to experiments in figure 10 (also compare with figure 8) with a good agreement except for bubbles of radius $R > 5a$, as expected considering the approximation (2.3) we used for the bubble geometry.

2.3. *Cell size and frequency*

2.3.1. *Destabilization frequency*

As explained in § 2.2.3, the neck in the pinching region at the bubble foot is liable to be destabilized by a Bénard-Marangoni mechanism driven by the surface tension gradient $\Delta\sigma/l$ across the pinching. This gradient is equilibrated, in the mean, by the tangential viscous stresses in the neck, leading the drainage velocity u in (2.16). But since both the thickness $h(s)$ and surface tension have a positive gradient along the coordinate s tangent to the bubble profile, the equilibrium in (2.16) is obviously unstable.

From the neck at $s = 0$ in the direction to the bubble pole, the thickness profile in the pinching region is approximately (see figure 9)

$$h(s) \simeq \frac{h}{l}s. \tag{2.19}$$

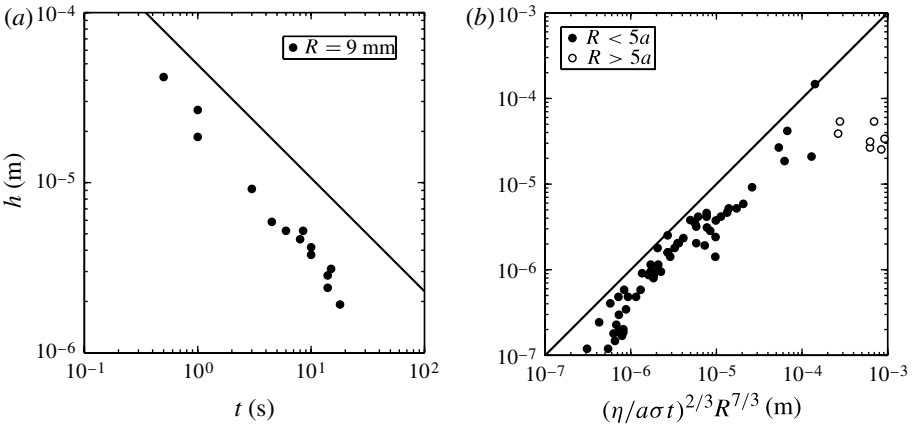

FIGURE 10. Bubble cap thickness h (•) versus time t elapsed since the emergence of the bubble at the bulk surface, and comparison with the thickness evolution law (2.18) (—). Thickness h is measured from the hole receding velocity $V = \sqrt{2\sigma/\rho h}$ (see § 4) when the bubble cap naturally punctures. (*a*) For bubbles of the same cap radius: $R = 9$ mm. (*b*) For bubbles of various radii R ranging from 1 to 25 mm and times t ranging from 5×10^{-2} to 30 s. No measurement has been discarded. Measurements on bubbles so large that (2.3) and thus (2.18), does not apply any more are identified by white-filled circles (○).

In that reference frame, the velocity of the draining liquid is $-u$ (directed towards the liquid bulk). Denoting by $\xi(t)$ the position of the neck along s, we see that from the perturbed equilibrium in (2.16)

$$\frac{\eta}{\sigma}(u + \dot{\xi}) \sim -\left(\frac{h - h(\xi)}{R}\right)^{3/2} \tag{2.20}$$

we have, from (2.19), the growth rate $\dot{\xi}/\xi$ of the perturbed position of the neck. This instability thus brings depleted portions of the film into the bubble cap at a frequency

$$f_0 = \frac{\dot{\xi}}{\xi} \sim \frac{\sigma}{\eta}\frac{h}{R^2} \tag{2.21}$$

or, making use of (2.18)

$$f_0 \sim \frac{\sigma}{\eta a}\left(\frac{R}{a}\right)^{1/3}\left(\frac{\eta a}{\sigma t}\right)^{2/3}. \tag{2.22}$$

The above relationship, measured from the bubble shown in figure 11 to last more than 40 s, is quantitative up to proportionality factor of 6 (figure 12).

2.3.2. *Destabilization size*

The perturbations from the neck can grow provided they are not damped too fast. When they escape from the pinching region, the dominant factor is no longer the viscous stress across the film, but rather the friction between the moving cells themselves. Therefore, if λ_0 is the size of a structure escaping the pinching region with amplitude ξ at velocity $\dot{\xi}$ towards the bubble cap, the typical stress in the film plane

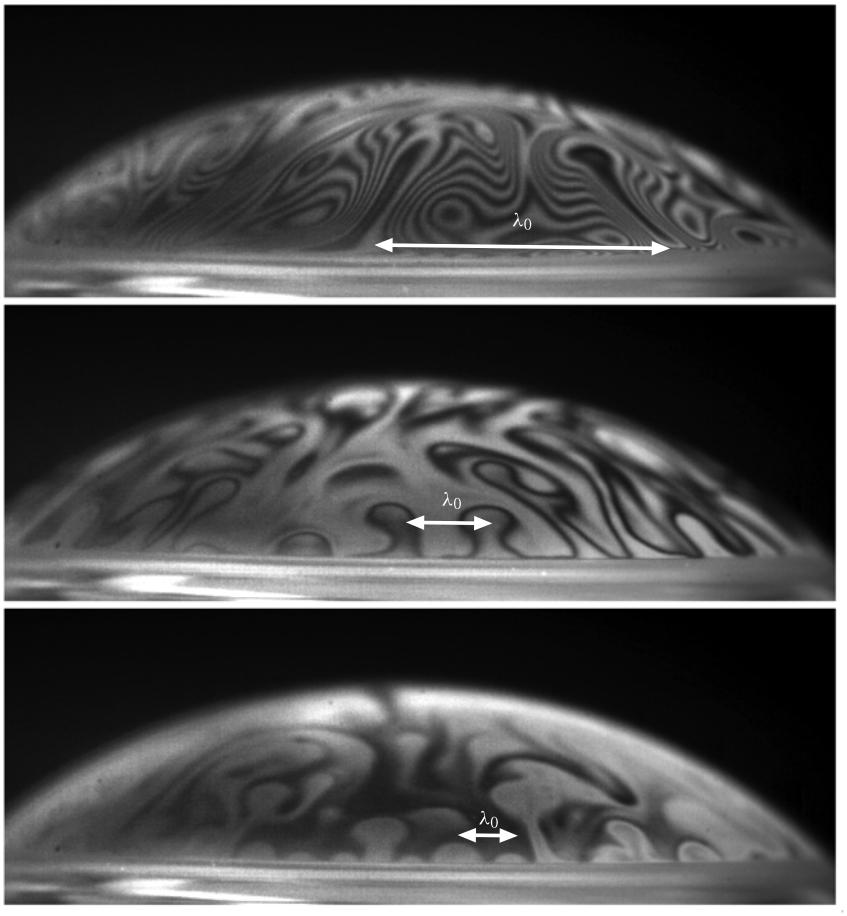

FIGURE 11. Evolution of the marginal regeneration convection cell wavelength as time elapses (sodium lamp at 589 nm). The bubble radius is $R = 5.7$ mm. From top to bottom respectively 2, 19.5 and 39 s has elapsed after the bubble has emerged at the surface.

that the driving force $\Delta\sigma$ has to overcome is $\eta\dot{\xi}/\lambda_0$, leading to the force balance

$$\frac{\eta\dot{\xi}}{\lambda_0}h \sim \frac{\Delta\sigma}{l}\xi \tag{2.23}$$

which, with $f_0 = \dot{\xi}/\xi$ given in (2.21), and $\Delta\sigma/h \sim \sigma/R$, provides

$$\lambda_0 \sim R\left(\frac{h}{R}\right)^{3/2} \tag{2.24}$$

or, again making use of (2.18)

$$\frac{\lambda_0}{R} \sim \frac{\eta a}{\sigma t}\left(\frac{R}{a}\right)^2. \tag{2.25}$$

It has to be stressed that, if (2.25) implies a dependence in time for λ_0 ($\propto t^{-1}$) which compares well with the observations reported in figure 12, it anticipates an absolute value for λ_0 smaller than the wavelengths actually observed by several

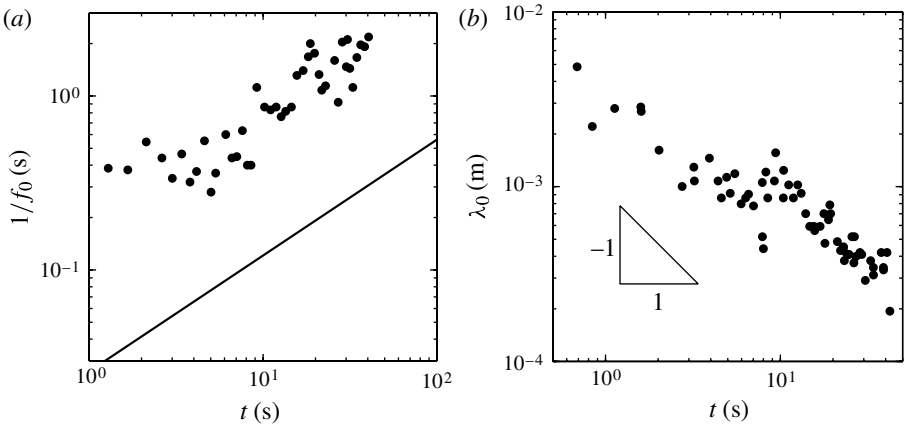

FIGURE 12. (*a*) Marginal regeneration convection cell emission period f_0^{-1} (•) measured on the bubble with $R = 5.7$ mm shown on figure 11 versus time t spent since the bubble formation. The line represents the law (2.22). (*b*) Evolution of the wavelength as defined on figure 11 for the same bubble (•). The slope of the power law $\propto t^{-1}$ of (2.25) is shown for comparison.

orders of magnitude. This is mostly due to the way we have represented the driving force of the instability. Away from the pinching zone towards the bubble pole, the surface tension gradient falls steeply from $\Delta\sigma/l$ to the much smaller magnitude ρgh (i.e. exactly stably counterbalanced by the film weight). The wavelength selection is precisely operated in this crossover region, characterized by an effective tension gradient intermediate between these two extremes, hence the major overestimate of $\Delta\sigma$ in absolute value in the balance of (2.23), and the corresponding underestimate of λ_0.

3. Puncture

With a fair representation of the film thickness h evolution in time to hand, and of the dynamics of the unstable structures at its foot, we now turn to the central question of the film thickness h_b *at the onset of bursting*. That question reduces to the determination of the bubble lifetime at the interface. As seen from figure 10(*a*), where time t is precisely the natural bubble lifetime for a selected set of identical bubbles generated exactly in the same way in the same water, this lifetime is quite distributed. The broad character of the lifetime distribution is general for films bursting naturally; it is known for natural bubbles (see for example Zheng *et al.* 1983) and is reminiscent of the stochastic nucleation process activated by rare events, an idea we will develop further.

Nevertheless, distributed though the lifetime may be, its average strongly depends on the bubble radius R, in a consistent and reproducible way. Bubbles burst by the nucleation of a hole in the vicinity of their foot (see e.g. figures 15, 17 and 18 below), and recording the hole opening velocity gives access to the film thickness at bursting h_b. Figure 13 shows our measurements together with those of Spiel (1998), both collapsing and suggesting that

$$h_b \simeq \frac{R^2}{\mathscr{L}} \tag{3.1}$$

where the length $\mathscr{L} \simeq 20$ m needs to be understood.

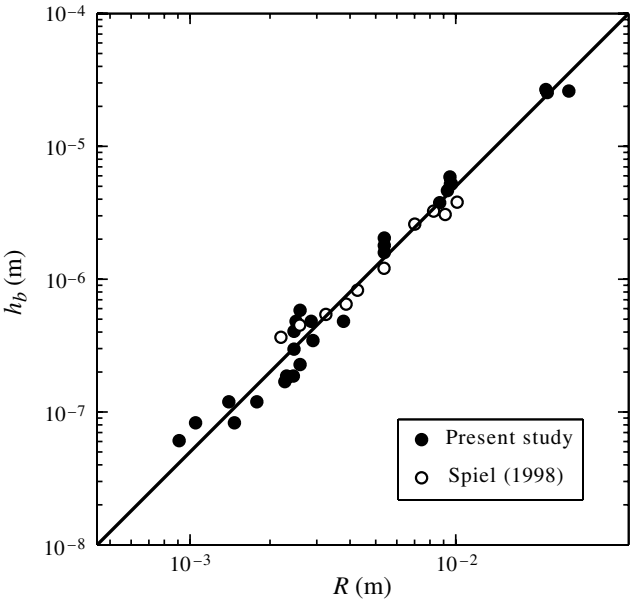

FIGURE 13. Thickness h_b at which bubbles spontaneously burst versus the cap radius R from our measurements (•) and those of Spiel (1998) (○). The line is $h_b = R^2/\mathscr{L}$ with $\mathscr{L} \simeq 20$ m (see (3.1)). Spiel's values were originally expressed in terms of the air cavity equivalent sphere radius; we converted them into R using the numerical bubble geometries.

3.1. *The traditional picture of soap films: thermal activation*

We have explained how the experimental law (3.1) does not apply to the extensively studied case of bubbles made out of highly concentrated soap solutions. In that context, marginal regeneration is known to be damped very rapidly due to the high surface viscosity caused by the large surfactant concentration (Bruinsma 1995). The drainage rate is therefore that of a Poiseuille flow over the whole bubble cap described by (2.9). The film is slightly thinner at the cap pole and it typically punctures there, when the film thickness h is of order a few tens of nanometres, say typically 10 nm. For such small thickness, the film is sensitive to thermal fluctuations (Bouchiat & Meunier 1971; Casteletto *et al.* 2003). Indeed, a hole through a film of thickness h opens only if its diameter $2r$ is larger than h. For a smaller hole, the in-plane curvature $\sim 1/r$ is larger than the curvature in the perpendicular plane $\sim 1/h$ and the hole closes. The nucleation of a hole across a film therefore requires that the interfacial area be transitorily increased by a minimal quantity of order h^2, corresponding to an energy barrier σh^2. The lifetime t of a film of area Σ subjected to energy fluctuations of mean W can therefore be expressed according to the standard Boltzmann–Kramers–Eyring estimate (Van Kampen 1981)

$$t \sim \frac{1}{f}\frac{h^2}{\Sigma}\exp\left(\frac{\sigma h^2}{W}\right) \tag{3.2}$$

where f is a frequency factor expressing the number of trials per unit time and per potential nucleation site, h^2/Σ is the number of such nucleation sites, and the exponential is an efficiency factor. Considering thermal fluctuations, the typical energy is $W = k_B T \sim 10^{-21}$ J and the frequency factor f is a molecular time of

order $k_BT/\hbar \sim 10^{12}$ s^{-1} (Maris 2006), where k_B and $\hbar$ are the Boltzmann and the Planck constants respectively. A lifetime t, of say 1 s, thus corresponds to a film of thickness $h \sim 1$–10 nm consistent with the expected value for very thin films, such as Newton black films (Casteletto *et al.* 2003). This scenario however predicts non-physical lifetimes for films thicker than a few tens of nanometres at room temperatures while bubble films are 1–10 microns thick. It in addition predicts a logarithmic dependence of the bursting thickness h_b on the bubble radius R, in clear contradiction with the experimental trend in (3.1).

3.2. *The role of marginal-regeneration-induced turbulence*

There is another source of agitation within the bubble cap film, which does not have a thermal origin, namely the turbulent motions generated by the marginal regeneration. They were measured in suspended vertical water films, in order to make visualization easier. By pulling a rigid frame out of a water bulk, we formed rectangular films 10 cm wide and 10 mm high (meniscus included) whose bottom side was connected to the bulk via the meniscus, like that of a bubble, and with the lateral and top sides connected to the frame. We focused on a narrow subpart of that horizontal width only, far from both lateral edges in order to limit their influence. The surface of the liquid bulk was initially seeded with micrometric particles, and the flow measurements have been made by particle image velocimetry (Meunier & Leweke 2003). A typical instantaneous velocity pattern is presented in figure 14. The mean kinetic energy of the flow decreases exponentially in time suggesting that surface friction is responsible for damping the motion (Xia, Shats & Falkovich 2009). Its maximal value is observed once the initial motion due to the film formation has been dissipated and its magnitude per unit film area is $\rho\langle u^2 + w^2\rangle \sim 1$ J m^{-3}. The film thickness measured at film bursting, roughly 2.5 s after its formation, was $h = 18$ μm. Using this lower bound, the typical kinetic energy within the volume h^3 is of order $W \sim \rho\langle u^2 + w^2\rangle h^3 \gtrsim 10^{-14}$ J. This value should be compared with the required energy barrier $\sigma h^2 \sim 10^{-11}$ J. In this first rough estimate, owing to thickness uncertainty and to a logarithmic pre-factor (see (3.2)) of order $\ln(h^2/\Sigma f) \sim \ln(h^3/\Sigma\sqrt{\langle \boldsymbol{u}^2\rangle}) \sim -20$, both energy scales do not seem to be strongly incompatible, and one could conclude that turbulent agitation is likely to provoke puncture.

However, a closer look discards marginal-regeneration-driven turbulence alone as a strong enough phenomenon to puncture the film. One indeed needs to consider velocity fluctuations at the scale of the hole nucleus h itself, rather than the large scale fluctuations $\sqrt{\langle \boldsymbol{u}^2\rangle}$ alone: global translation will not alter the film, whereas localized stretching will. This condition is much more restrictive since now in order to provoke film puncture, velocity differences $\sqrt{\langle \delta\boldsymbol{u}^2(h)\rangle}$ at the scale h must be considered, and should be of the same order as the film receding velocity $V = \sqrt{2\sigma/\rho h} \sim 1$–$10$ m s^{-1}. This condition is very far from being fulfilled in naturally agitated films, as we show quantitatively in appendix C.

3.3. *The role of convection cells*

The detailed mechanism of thick film rupture thus remains unclear. However, several experimental observations substantially constrain the possibilities:

(*a*) the film thickness at the bursting h_b depends markedly on the bubble cap radius R (equation (3.1));

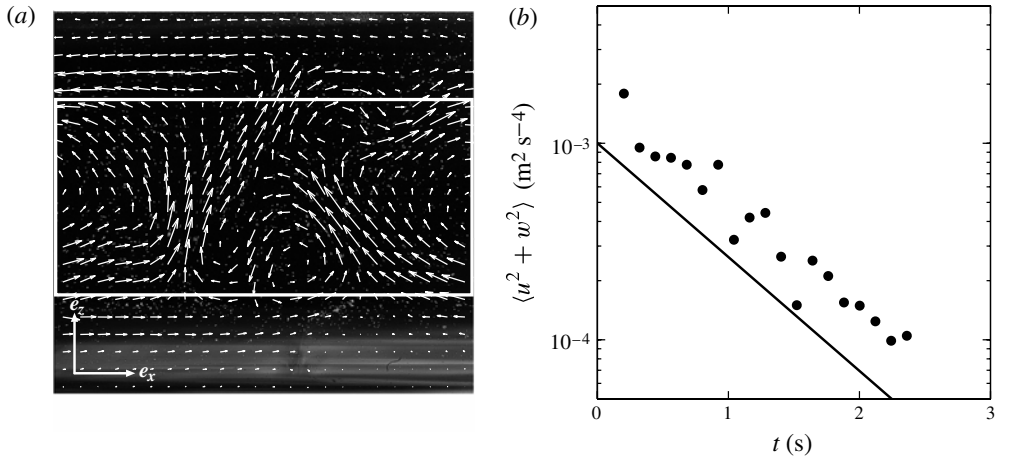

FIGURE 14. (*a*) Typical velocity field induced by marginal regeneration in a flat vertical film formed by pulling a frame out of a water bulk (similar to that of figure 6). The bottom brightest portion and the top portion, where velocities are horizontal, are the two meniscii connecting the film to the bulk and to the top of the frame respectively. Image width is 10.8 mm and $\sqrt{\langle \boldsymbol{u}^2 \rangle} = 7.2$ cm s^{-1}. Velocities are obtained by particle image velocimetry; only one out of four velocity vectors is plotted to make visualization easier and statistics are exclusively computed on the velocity field contained in the white frame which corresponds to the film portion. (*b*) Mean kinetic energy $\langle u^2 + w^2 \rangle$ over the film versus time t elapsed since film formation.

(*b*) this thickness h_b is independent of the precise content of the solution (as long as large soap concentrations are not involved) in the sense that our measurements with tapwater superimpose with those of Spiel (1998) using seawater (figure 13);

(*c*) most important, and by contrast with soap bubbles where puncture occurs at the cap pole, tapwater bubbles preferentially puncture in the vicinity of the cap foot, i.e. close to the meniscus that connects it to the bulk, in the unstable region covered with the convection cells described in § 2.3. Among 25 observed bubbles of cap radius $R = 5$ mm, puncture occurred 22 times between $\theta = 25°$ and the bubble foot in $\theta_c = 30°$. In other words, almost 90 % of nucleation events occurred over less than 30 % of the whole cap surface: that which is the closest to the bubble foot, as seen in figures 15 and 17;

(*d*) the puncture preferentially occurs at the centre of the unstable convection cells (figure 15), and the hole opening velocity V is larger than any other velocity in the bubble.

The dynamics of the marginal regeneration, which has enabled an appropriate description of the bubble cap thinning, and which is responsible for the bubble foot agitation, is thus seemingly also at the root of the bubble bursting. We develop below arguments which do not explain why the film punctures, but which appropriately describe how, explaining in particular the structure of (3.1).

New cells are injected at the bubble foot every period f_0^{-1}. The evidence listed above suggest that puncture will most certainly occur within a cell, at its centre, but that this process is extremely inefficient: only about one out of a thousand or ten thousands

FIGURE 15. Spontaneous bursting at the foot of a flat water film (interference fringes visualized by a monomode argon laser at 488 nm). Nucleation is seen to occur around a convection cell: the paradigm situation in the bursting of bubbles. Image height is 3 mm and time lapse between the two images is 1/3000 s. The film receding velocity is $V = 2.8\ \mathrm{m\ s^{-1}}$ corresponding to a thickness $h = 20\ \mu\mathrm{m}$.

cells will puncture, leading to the bubble burst. We call

$$\epsilon = O(10^{-4}\text{–}10^{-3}) \tag{3.3}$$

the efficiency of one cell puncture (independent of time) so that $\epsilon f_0 \delta t$ is the probability that one cell has punctured within a time interval δt. There are, at the base perimeter $P \sim R^2/a$ of a bubble, P/λ_0 cells on average at a given time. The probability $p(t)\delta t$ that puncture occurs within δt on the bubble is thus extensive to both the efficiency factor ϵ and the number of cells (like in (3.2), the cells are assumed to be independent and therefore to contribute in an additive fashion to the bursting probability) present at a given time

$$p(t)\delta t \sim \epsilon \frac{P}{\lambda_0} f_0\, \delta t. \tag{3.4}$$

Conversely, $1 - p(t)\delta t$ is the probability that no cell has punctured the bubble within δt, so that the probability $Q(t)$ that the bubble has not burst at time t is

$$Q(t) = \prod_{t'/\delta t'=0}^{t/\delta t'} [1 - p(t')\delta t'] \underset{\delta t' \to 0}{\longrightarrow} \exp\left(- \int_0^t p(t')\, \mathrm{d}t' \right). \tag{3.5}$$

If $q(t)$ is the distribution of the bubble lifetime, it follows that

$$q(t) = -\partial_t Q(t) = p(t)\ \exp\left(- \int_0^t p(t')\, \mathrm{d}t' \right). \tag{3.6}$$

Given the scaling laws for f_0 and λ_0 in (2.22) and (2.25), the bursting probability per unit time $p(t)$ is written as a weakly increasing function of time

$$p(t) = \frac{4}{3} \frac{t^{1/3}}{\tau_0^{4/3}} \tag{3.7}$$

with

$$\tau_0 = \frac{(4/3)^{3/4}}{\epsilon^{3/4}} \frac{\eta a}{\sigma} \left(\frac{R}{a} \right)^{1/2} \tag{3.8}$$

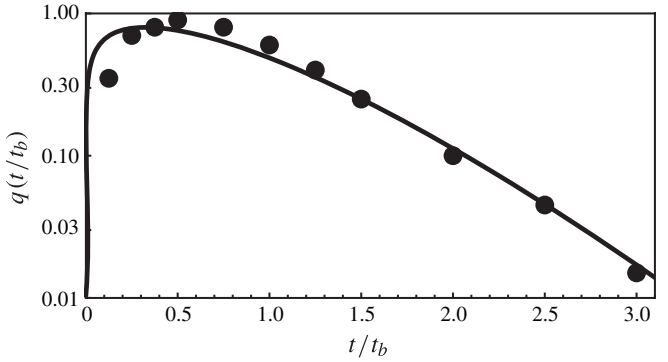

FIGURE 16. Mean bubble lifetime distribution $q(t)$, averaged from the lifetime distributions of bubbles ranging from 1.2 to 7.4 mm in diameter, adapted from figures 5, 6 and 7 in Zheng, Klemas & Hsu (1983) and compared to (3.9) (the line).

so that

$$q(t) = \frac{4}{3}\frac{t^{1/3}}{\tau_0^{4/3}} \exp\left(-\left(\frac{t}{\tau_0}\right)^{4/3}\right) \tag{3.9}$$

which presents an algebraic increase at small time ($\propto t^{1/3}$), and a faster than exponential fall off at large times (identical to that of $Q(t)$), consistently with the distributions reported in Zheng *et al.* (1983), as seen in figure 16. The mean bubble lifetime, or bursting time, which we call t_b, is

$$t_b = \int_0^\infty t\, q(t)\, \mathrm{d}t = \int_0^\infty Q(t)\, \mathrm{d}t \tag{3.10}$$

that is

$$t_b = \Gamma(7/4)\, \tau_0 \approx 0.92\, \tau_0. \tag{3.11}$$

The bursting time is dimensionally set by the capillary viscous time $\eta a/\sigma$ (of the order of 10^{-5} s for water), and is larger by several orders of magnitude owing to the factor $\epsilon^{-3/4}$, reaching up to seconds. It is proportional to the square root of the bubble size, in agreement with our observations and those in Zheng *et al.* (1983) where the bubble mean lifetime is seen to increase with R for small bubbles. From (2.18), one finally obtains the (mean) bubble cap thickness at the bursting time as

$$h_b \sim a\epsilon^{1/2}\left(\frac{R}{a}\right)^2 = \frac{R^2}{\mathscr{L}} \tag{3.12}$$

with the length $\mathscr{L}$ solely function of the capillary length scale, and differing from it by a very large amount depending on the puncture efficiency factor ϵ

$$\mathscr{L} \sim \frac{a}{\epsilon^{1/2}}. \tag{3.13}$$

As seen in figure 13, this law accounts very well for our, and Spiel (1998)'s, experimental measurements.

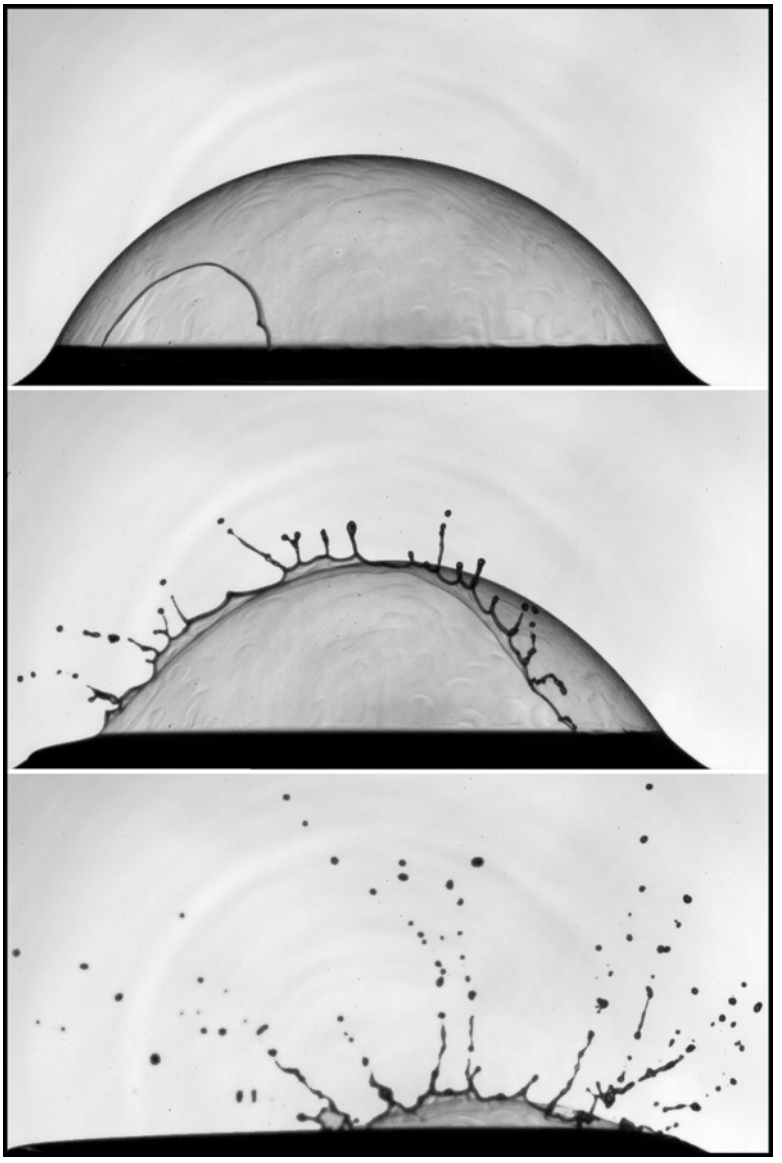

FIGURE 17. Spontaneous bursting of a bubble at the surface of a water bulk. Convection cells can be seen all over the cap via the light refraction induced by the thickness modulations. $R = 10$ mm, $h = 3.1$ μm and time between images is 1 ms.

4. Fragmentation dynamics

The detailed study of the bubble cap drainage and its puncture culminates in the scaling law (3.12) linking the two length scales characterizing a bubble, on average, namely the thickness of its cap $h \equiv h_b$ and its radius R, at the time it bursts. We now turn to the sequence of events occurring after a hole has punctuated the bubble cap, aiming to understand the products of the bursting, that is the subsequent drops, and their size distribution.

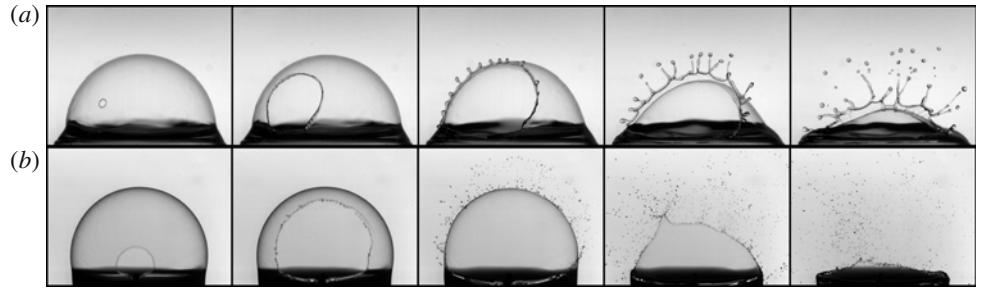

FIGURE 18. Bursting of two bubbles of comparable radii R and distinct thicknesses h. (a) $R = 14$ mm, $h = 36$ μm and time between images is 2.5 ms. (b) $R = 11.5$ mm, $h = 1.2$ μm and time between images is 0.67 ms.

4.1. *Mechanisms and mean drop size*

Once a hole nucleates through the bubble cap, the resulting fragmentation dynamics is very fast compared to the slow drainage dynamics described before. This initial hole extends circularly, driven by surface tension, at the constant Taylor–Culick velocity $V = \sqrt{2\sigma/\rho h}$ (Culick 1960) and is bordered by a rim collecting the liquid film. The constant velocity V is reached within a capillary time based on h, which is short compared to the following destabilization mechanisms. The rim receding motion follows the curved bubble cap (the validity of this assertion is discussed further) and thus imposes a centripetal acceleration

$$\gamma = \frac{V^2}{R} \tag{4.1}$$

to the rim. The latter thus suffers an inertial destabilization of a Rayleigh–Taylor type, which leads to the formation of regularly spaced ligaments as figures 17 and 18 show. Remarkably, the instability wavelength λ is the geometrical mean of the two length scales of the problem R and h (Lhuissier & Villermaux 2009) and the instability growth time τ is the capillary time based on that combined length

$$\lambda \sim \sqrt{\frac{\sigma}{\rho\gamma}} \sim \sqrt{Rh}, \tag{4.2a}$$

$$\tau \sim \left(\frac{\sigma}{\rho\gamma^3}\right)^{1/4} \sim \sqrt{\frac{\rho\ (Rh)^{3/2}}{\sigma}}, \tag{4.2b}$$

relationships which are both consistent with experiments, as seen in figure 19.

Ligaments spaced by λ are then stretched out by centrifugation, and are soon resolved into disjointed droplets by a Plateau–Rayleigh destabilization. The capillary time associated with this ultimate fragmentation being short compared to τ, the time $t_{1^{st}}$ for the first drops to be ejected is proportional to τ and indeed, we observe that

$$t_{1^{st}} \simeq 3\,\tau \tag{4.3}$$

as seen in figure 19. Note that this inviscid theory applies to water. Viscous liquids present a much slower destabilization, since both Rayleigh–Taylor and capillary instabilities are slowed down by viscosity (see e.g. Bird *et al.* 2010 for a study of that limit).

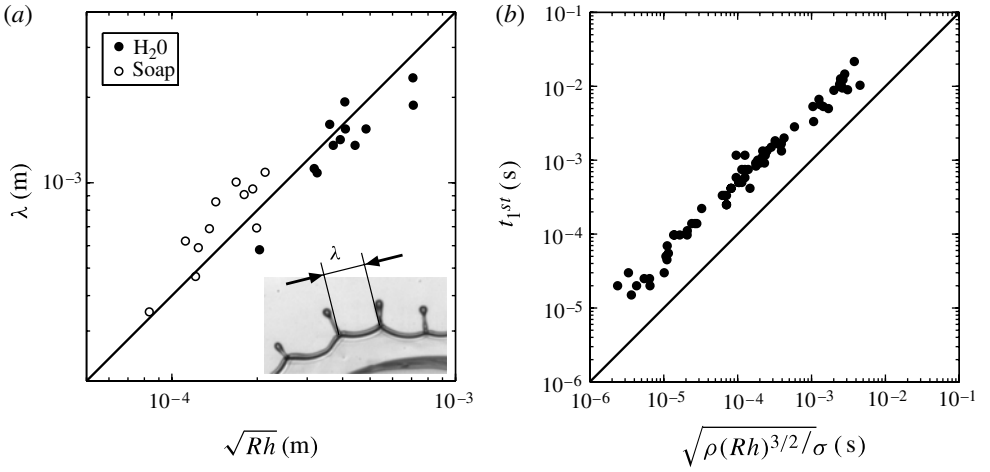

FIGURE 19. (*a*) Ligament spacing λ for bubbles in tapwater (•) and soap saturated solution (○) (a solution of tapwater and 'Dreft' by Procter & Gamble above the critical micelle concentration having a surface tension of 25 mN m^{-1}) versus the expected scale law of (4.2*a*), up to a factor 3. (*b*) Delay $t_{1^{st}}$ before first drop is released versus τ defined in (4.2*b*).

The droplet mean diameter $\langle d \rangle$ in the resulting spray is set by the ligament diameter when drop pinch-off occurs, as is known from the capillary instability of moderately corrugated threads (Eggers & Villermaux 2008). The ligament diameter is observed to remain roughly constant from the onset of their formation to their fragmentation since their stretching by centrifugation is compensated by the film flow permanently feeding them. The average drop diameter $\langle d \rangle$ is thus directly proportional to the rim diameter at the onset of ligament formation, that is to say after a rim recession time τ and then

$$\langle d \rangle \sim \sqrt{V\tau h} \sim R^{3/8}\, h^{5/8}. \tag{4.4}$$

Figure 20 shows a reasonable agreement with that prediction, with a slight departure for the smallest bubbles.

4.2. *Range of relevant bubble sizes and number of drops per bubble*

The number of drops N produced at each bursting event depends on the bubble shape, that is on R/a (§ 2). As long as R is large enough the ejection time $t_{1^{st}}$ is short compared to the rim recession time over the half-cap $R\theta_c/V \sim R^2/aV$. Using the expressions for V and $h_b \simeq R^2/\mathscr{L}$, one obtains the limiting bubble radius for film drop production:

$$R_i \simeq (2 \times 3^5 \times a/\mathscr{L})^{1/3}\ a \simeq 0.4\, a. \tag{4.5}$$

Bubbles smaller than this critical value are expected to produce no film drops, and the jet drop mechanism prevails in that case. The above order of magnitude $R_i \simeq 1.1$ mm is consistent with previous experimental estimates by Resch & Afeti (1991) and Spiel (1998) who found $R_i \simeq 0.6$ and 1.2 mm respectively for bubbles in seawater.

At the other extreme, the film drop production mechanism is also limited for large bubbles since they deflate before the cap recession is completed, and rim instability initiated. An estimation of the bubble deflation time τ_{def} can be made for large bubbles assuming for simplicity that the air cavity remains a half-ball with volume $2\pi R\,(t)^3/3$

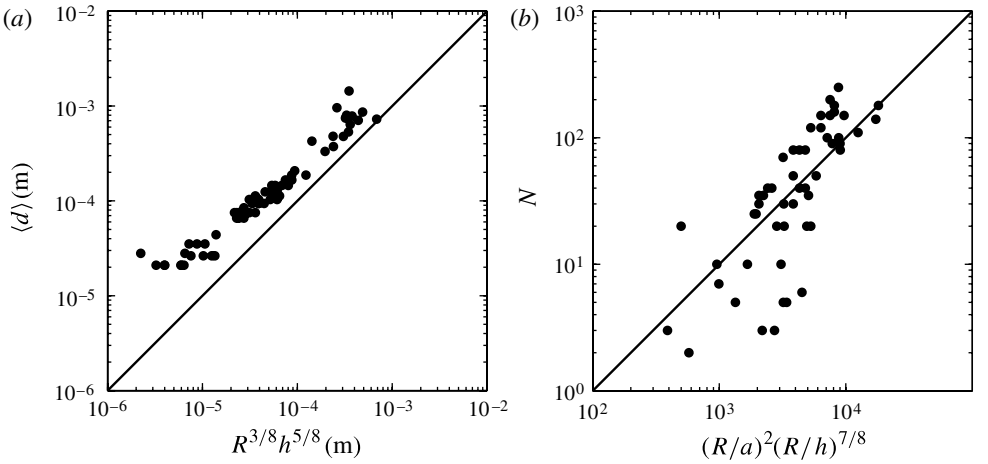

FIGURE 20. (*a*) Mean drop size $\langle d \rangle$ versus prediction of (4.4). (*b*) Number N of drops produced per bubble versus prediction of (4.11). The line is $y = 10^2 x$.

during collapse, where $R(t)$ is now the decreasing radius of the bubble since puncture. The pressure inside the bubble $4\sigma/R(t)$ drives a potential air flow from the bubble cavity to the outer atmosphere with velocity $\sqrt{2\sigma/\rho_a R(t)}$, where ρ_a is the constant air density. The hole in the cap through which the air escapes has a current section $\pi\,(Vt)^2$. By conservation of the air volume, we have

$$\frac{\mathrm{d}}{\mathrm{d}t}R^3 = -3\sqrt{\frac{2\sigma}{\rho_a R}}\,(Vt)^2 \tag{4.6}$$

giving

$$R(t) = R(0)\left[1 - \left(\frac{t}{\tau_{def}}\right)^3\right]^{2/7} \tag{4.7}$$

where

$$\tau_{def} = \left(\frac{6}{7}\right)^{1/3}\frac{R(0)}{V}\left(\frac{\rho_a R(0)}{\rho\, h}\right)^{1/6}. \tag{4.8}$$

The radius shrinks to zero in finite time (see Dupré 1869, p. 353, for the similar problem of the soap bubble emptying through a straw). Figure 21 shows the evolution of the cap radius $R(t)$ of a large bursting bubble during collapse, compared with the law expected from (4.7) showing that τ_{def} indeed gives an accurate approximation of the experimental deflation time. Note that the influence of deflation is in fact complex, since it first increases the cap curvature at its apex, thus enhancing the rim centrifugation. However, since the bubble meniscus position is unchanged during rim recession, the cap flattens at larger times and centrifugation is inhibited. This deflation effect leads to an upper cut-off radius R_s for film drop production, defined according to $R_s\theta_c/V \simeq \tau_{def}$, that is

$$R_s \simeq \left(\frac{2^8 \times 3^5}{7^2}\frac{\rho_a}{\rho}\frac{\mathscr{L}}{a}\right)^{1/7} a \simeq 3.8\,a. \tag{4.9}$$

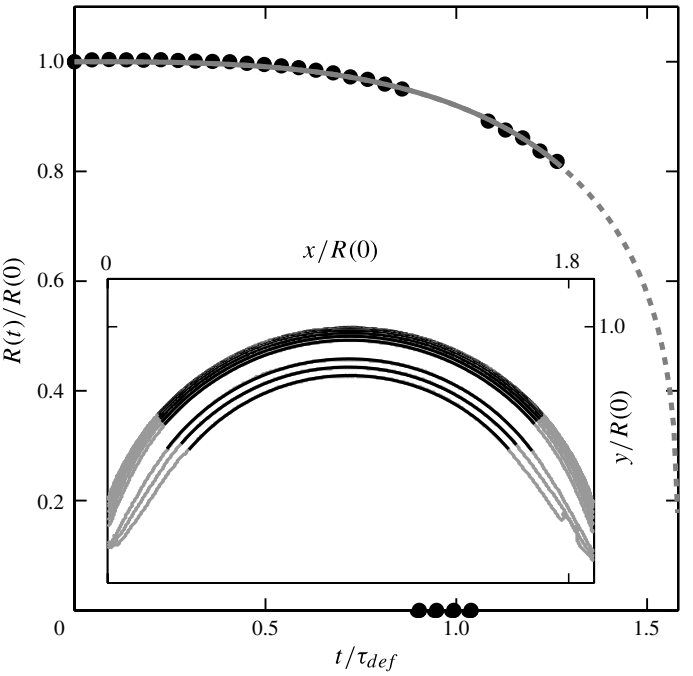

FIGURE 21. Bubble radius $R(t)$ (•) versus time t since puncture. The line is the best fit by the evolution law (4.7). The experimental deflation time is thus found to be approximately 1.6 times the characteristic time τ_{def} defined in (4.7) ($R(0) = 7.7$ mm, $V = 2.85$ m s^{-1} and $\tau_{def} = 2.2$ ms). Inset: bubble cap profiles. The red parts show the portion of each profile that was used for the determination of R. Radii have been measured until half-cap recession. Missing dots and profiles around $t/\tau_{def} = 1$ correspond to not readable profiles hidden by the ligaments.

For bubbles with radii between R_i and R_s, the corresponding number of drops formed by burst N can be estimated assuming that the whole liquid cap, of volume

$$\Omega \sim \frac{R^4 h}{a^2}, \tag{4.10}$$

is fragmented into droplets of diameter $\langle d \rangle$. As will be seen in § 5, because the ligaments are weakly corrugated, the dispersion of drop sizes for a single bursting event is quite small, and $\langle d^3 \rangle$ is of the same order as $\langle d \rangle^3$. Therefore, N can be written

$$N \sim \frac{\Omega}{\langle d \rangle^3} \sim \left(\frac{R}{a}\right)^2 \left(\frac{R}{h}\right)^{7/8}. \tag{4.11}$$

This formula overestimates the number of drops actually observed in our experiments (figure 20*b*) because the assumption that the whole volume Ω is converted into drops is obviously a simplification. It however describes well the dependence of N on the cap radius R (if we except the particularly small bubbles on the left-hand side of the graphics for which only a small portion of the cap volume Ω is expected to be fragmented according to the discussion leading to the definition of R_i in (4.5)), which is enough for our purpose since we will only need to consider relative productions in the range $R_i \leqslant R \leqslant R_s$ in what follows. It is also worth noting that considering $h_b \propto R^2$

provides

$$N \propto R^{9/8} \tag{4.12}$$

from (4.11), showing that big bubbles produce more drops than smaller ones do. This trend is also consistent with previous observations in seawater which, however, present some discrepancies. Resch & Afeti (1991), using their own measurements and those of Blanchard & Sysdek (1988) that they reinterpreted, found an empirical power law $N \propto R^{1.5-1.8}$ while more recent measurements by Spiel (1998) show a weaker dependence on R, closer to $N \simeq bR + c$ with a cut-off at $R_i = -c/b \simeq 1.2$ mm as already mentioned.

4.3. *Culick's law on a curved film*

The rim receding velocity $V = \sqrt{2\sigma/\rho h}$ that we have used for computing the rim centripetal acceleration is strictly valid for a planar film where the motion is a translation along the film uniform tangential direction $\boldsymbol{e_t}$. It, however, remains valid for a film of constant radius of curvature R under a condition we discuss below, and which turns out to be fulfilled for the bubbles we are concerned with.

When the velocity of the rim is not constant in direction, its rate of momentum variation induced by the surface tension force operating tangent to the film splits into two components:

(*a*) that due to the liquid at rest in the film being collected into the rim and accelerated to the rim tangential velocity V, i.e. $\rho h V^2 \boldsymbol{e_t}$;

(*b*) that due to the liquid already in the rim and undergoing the centripetal acceleration $-(mV^2/R)\boldsymbol{e_n}$, where m is the current rim linear mass and $\boldsymbol{e_n}$ is the outer unit vector normal to the bubble.

The latter is of order of the former and needs to be considered only when

$$m \geqslant \rho h R, \tag{4.13}$$

that is to say when the rim has receded over a distance larger than R without ejecting any drops. That was observed only for bubbles of radius R larger than a few centimetres. For smaller bubbles, liquid is ejected from the rim all along the recession path and V is well represented by the planar prediction. The observed fact that the rim trajectory coincides with the bubble cap position is also consistent.

5. Aerosol production

5.1. *Single bubble spray*

The interpretation of the global spray production at the ocean surface requires knowledge of the drop size content from a single bursting bubble. We focused on relatively big bubbles with radius $R = 12$ mm formed at the top of a 20 mm diameter glass tube filled with water. This large radius was chosen for measurement precision, but the resulting fragmentation properties, in particular the shape of the drop size distribution $p(d)$, are generic for all bubble radii. Bubbles were rapidly inflated and their bursting was initiated by positioning a hydrophobic sand-coated needle at a fixed height above the tube. This allowed us to burst bubbles of the same radii and thicknesses and to accumulate precise statistics. This also allowed us to determine the puncture location on the bubble cap and have all the ligament fragments in the camera focus plane at the same time. Drop diameters d were measured on images taken late

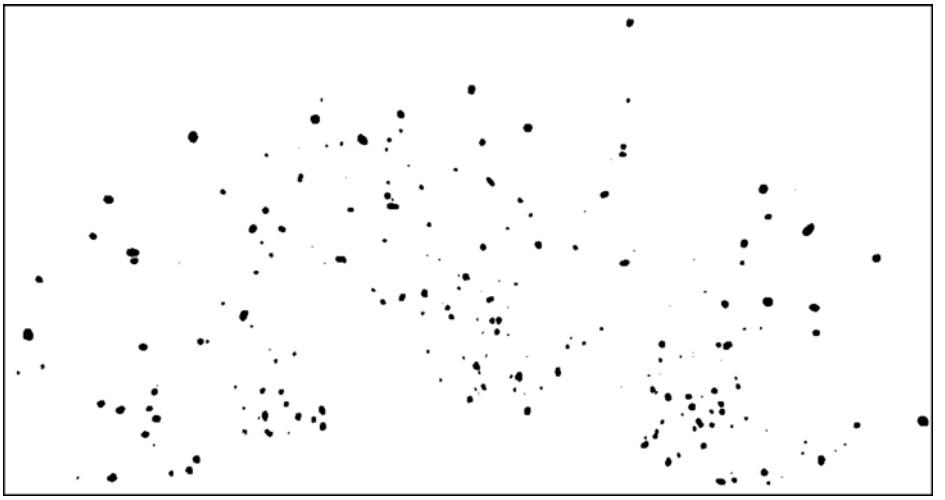

FIGURE 22. Example of a 210 drop population generated by a single bubble. The largest drops have a diameter of 500 μm.

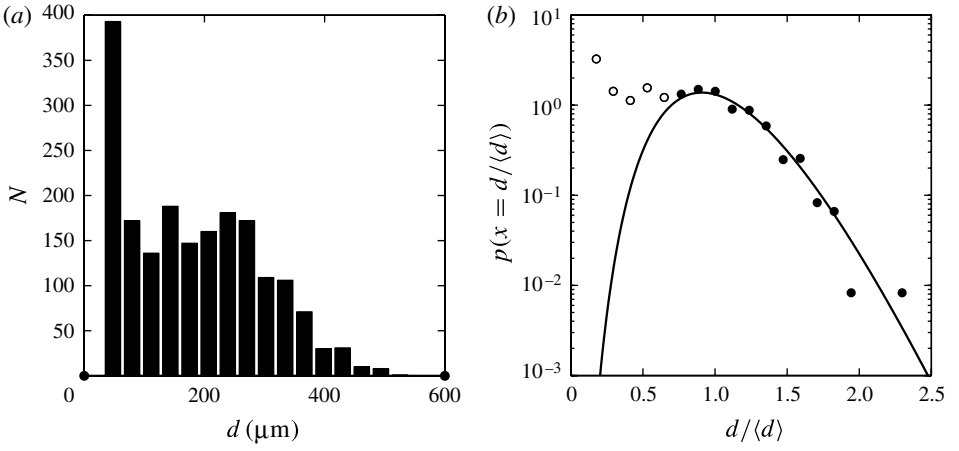

FIGURE 23. Distribution of drop diameters d resulting from the provoked bursting of 12 identical bubbles representing almost 2000 drops. (*a*) Original data (note that the size of a pixel corresponds to 32 μm and thus the relative weight of the two first bins is not necessarily relevant). (*b*) Normalized drop size distribution (dots) and fit by a Gamma distribution (see (5.1)) of order $n = 11$. Only black points (•) corresponding to $d > 5$ px are used for the normalization and the fit.

enough after ligament breakup for all drops to have relaxed to a nearly spherical shape. An example is shown in figure 22.

The drop size distribution measured on a set of 12 identical bubbles is presented in figure 23. With a resolution scale of 30 μm, and with largest drops of 500 μm, the distribution presents two characteristic parts: a roughly uniform fraction of small sizes, and a bell-shaped fraction with steep tail for larger sizes. This latter fraction is very

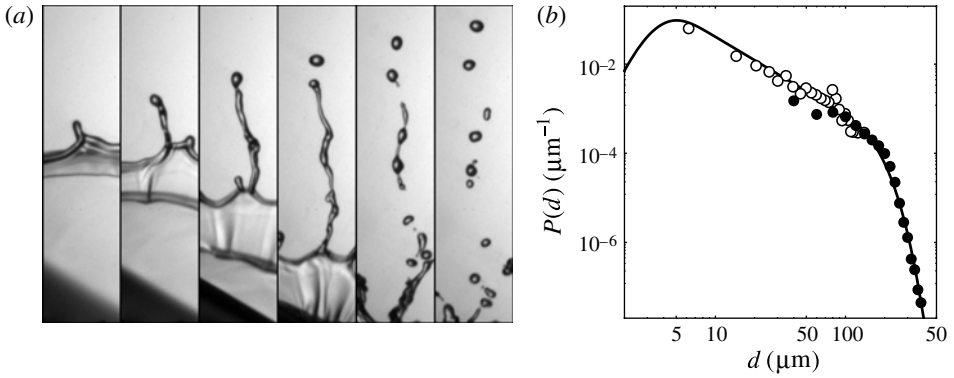

FIGURE 24. (*a*) Fragmentation dynamics of a centrifuged ligament resulting from the bursting of a bubble. (*b*) Global experimental drop size distribution $P(d)$ estimated by combination of Wu, Murray & Lai (1984)'s (•) and Preobrazhenskii (1973)'s (○) *in-situ* measurements. They are compared to (5.4) with $R_i = 0.4a$ and $R_s = 3.8a$ (—). Note that Wu *et al.* (1984)'s and Preobrazhenskii (1973)'s are partial distributions that are not 'vertically positioned' relative to each other; we combined them so that they coincide in their common drop size range. The compound distribution is not normalized on our graph in order to permit comparison with (5.4).

well described by a Gamma distribution

$$p\left(x = \frac{d}{\langle d\rangle}\right) = \frac{n^n}{\Gamma(n)}\, x^{n-1}\mathrm{e}^{-nx} \tag{5.1}$$

where $\Gamma(n) = \int_0^\infty t^{n-1}\mathrm{e}^{-t}\,\mathrm{d}t$ is the Gamma function. This size distribution is the signature of ligament-mediated fragmentation (Villermaux, Marmottant & Duplat 2004), those being, as in all atomization processes, the ultimate objects forming the drops, as figure 24 depicts. Small initial surface corrugations lead to smooth ligaments, and therefore to a quite narrow drop size distribution around the mean (we find $n = 11$ in figure 23, whereas a pure decaying exponential would have $n = 1$, and a Dirac delta function would correspond to $n \to \infty$ (see Villermaux 2007)).

The uniform portion of the size distribution for small d is a consequence of a secondary fragmentation process due to transverse impacts between adjacent ligaments. These impacts occur as the rim hole starts to shrink, when the rim has receded from more than half the initial sphere, and ligaments move closer to each other. This effect only concerns large bubbles since it imposes $\theta_c > \pi/2$ (see figure 4). We thus suspect that this small-d fraction of the measured distribution is due to the large bubble radius we have chosen, and that the drop size distribution for smaller bubbles will be close to a pure Gamma distribution. Besides, the observations of Spiel (1998) made from bubble radii ranging from 1.5 to 6 mm indicate a clear decrease of the drop size distributions $p(d)$ for small d.

5.2. *Global spray*

With a drainage model and a description of the fragmentation dynamics providing closed relationships linking h_b, N and $p(d/\langle d\rangle(R))$ to the bubble radius R we are now able to infer a global spray distribution $P(d)$ directly from knowledge of the bubble

size distribution at the ocean surface $q(R)$ as

$$P(d) = \frac{1}{N_0} \int_{R_i}^{R_s} \frac{q(R)\, N(R)}{\langle d \rangle (R)}\, p(d/\langle d \rangle (R))\, \mathrm{d}R, \tag{5.2}$$

simply expressing that the overall spray results from a weighted sum of the contributions from all bubbles between R_i and R_s. We indeed consider that the real phenomenon in nature involving many bubbles with different sizes, such as those produced in a foam by wave breaking in the ocean for instance, can be interpreted from the scenario we have established for a single isolated bubble, in a linearly additive fashion, and that no new effect arise from the proximity of the bubbles in the foam. Nearby bubbles may coalesce, and we argue in appendix D that the coalescence event just delays the onset of bubble bursting, without altering its features compared to those of an isolated bubble. We also assume in writing (5.2) that the droplets ejected from a given bubble in the bubble foam assembly will not interfere with the natural aging (drainage, spontaneous puncture) process intrinsic to a single bubble, or at least that these interferences, if they happen, are negligible.

The integration domain in (5.2) is bounded on both sides (§ 4). The lower bound $R_i \simeq 0.4\, a$ corresponds to a bubble cap extension θ_c so small that drop ejection cannot occur before rim recession ends, whereas the upper bound $R_s \simeq 3.8\, a$ corresponds to bubbles so large that their deflation is faster than the rim recession as we discussed in § 4.2.

Realistic bubble size distributions $q(R)$ at the sea surface must be estimated from separate measurements, such as those of Deane & Stokes (2002) for wave breaking. In the 1–10 mm bubble radius range corresponding to the film drop production range, these authors find that

$$q(R) \propto R^{-10/3}, \tag{5.3}$$

a law apparently insensitive to the precise way wave breaking has been initiated, and holding both for ocean and artificial laboratory waves. Thus, $q(R), N$ and $\langle d \rangle$ all follow power laws in R.

Defining the exponents α and β such that $q(R)N(R) \propto R^{-\alpha}$ and $\langle d \rangle (R) \propto R^{\beta}$, and introducing $\zeta = (\alpha - 1)/\beta$, the overall compound distribution $P(d)$ is written from (5.1) and (5.2)

$$P(d) = \frac{1}{N_0'}\, d^{-1-\zeta} \left[\Gamma_{inc}\left(n+\zeta, \frac{n\, d}{\langle d \rangle_s}\right) - \Gamma_{inc}\left(n+\zeta, \frac{n\, d}{\langle d \rangle_i}\right) \right] \tag{5.4}$$

where $\Gamma_{inc}(n, \tilde{d}) = \int_{\tilde{d}}^{\infty} t^{n-1} \mathrm{e}^{-t}\, \mathrm{d}t$ is the so-called incomplete Gamma function and $\langle d \rangle_i$ and $\langle d \rangle_s$ correspond to the mean drop size from bubbles of radius R_i and R_s respectively as defined in (4.4). According to (4.4), (4.11) and the measurements of Deane & Stokes (2002), we have $\zeta = 3/4$ leading to a distribution which behaves like

$$P(d) \propto d^{-(1+\zeta)} = d^{-7/4} \tag{5.5}$$

between the two cut-offs imposed by R_i and R_s. The compound distribution $P(d)$ is shown in figure 24(*b*) to superimpose extremely well on field measurements made by Preobrazhenskii (1973) and Wu *et al.* (1984).

6. Conclusion

We have described the complete sequence of events of the life and bursting of a bubble at the surface of a water pool, and we have underlined the relevance of

this process for understanding how aerosols are produced at the surface of the sea. This study has revealed a rich phenomenology, some of its aspects being completely understood, some other remaining obscure.

(*a*) We have considered bubbles whose radius ranges from a fraction, to a couple, of capillary length scales $a \simeq 2.7$ mm. A 'small' amount of surfactant on the bubble cap has large consequences: the lifetime of the bubble jumps from hundredths of a second (for pure water) to several seconds, up to tens of seconds.

(*b*) The marginal pinching at the bubble foot, and the inherent marginal regeneration phenomenon, are crucial to understand the thinning law of the bubble cap. The exchanges of the interstitial fluid in the cap with the liquid bulk are set by the pinch-off thickness which is slaved to that of the cap by its recurrent destabilization.

(*c*) The bubbles burst by nucleating a hole precisely in this marginal regeneration region (not at their pole, as opposed to soap bubbles); the holes nucleate at the centre of the convection cells, which therefore also appear as the objects responsible for the bubble bursting.

(*d*) Neither thermally activated noise, nor turbulence in the marginal regeneration region are strong enough to puncture the film. The energy levels associated with these effects are orders of magnitude below that required to puncture a hole.

(*e*) The film is typically thick at breakup: it is one to ten microns thick. Attractive Van der Waals forces are unlikely to operate in this range.

(*f*) Evaporation has not been considered. However, in exactly the same conditions as those of our bubble experiments, a layer of tapwater evaporates at a velocity of a hundredth of a micron per second (see figure 25), a rate which, owing to the typical bubble lifetime (seconds) and cap thickness (several microns), suggests that evaporation is a subdominant effect. Moreover, no definite trend has been observed in the bubble mean lifetime when the liquid bulk temperature was varied in the range 4–80 °C.

(*g*) The ultimate mechanism puncturing the film remains a mystery, and this is certainly a topic for future research. However, assuming that the phenomenon occurs in the marginal regeneration convection cells with a frequency associated with their rate of production, times a very small efficiency factor, accounts for the features of the bubble, in particular its mean lifetime and consequently the thickness of its cap, at bursting.

(*h*) The subsequent sequence of events, namely the hole opening velocity, its rim destabilization by a Rayleigh–Taylor mechanism, the formation of ligaments, their capillary breakup, and finally the distribution of the resulting fragment droplets within the range of bubble radii liable to produce fragments are clearly demonstrated, measured, and understood.

(*i*) Remarkably, a linear superposition of the contribution of a single bubble to the overall spray, in proportion to its relative occurrence at the surface of the sea given its radius represents very accurately the observed sea spray distribution.

Paraphrasing Michael Faraday's *Chemical History of a Candle* (Faraday 1861), we could conclude that: There is no better, there is no more open door by which you can enter into the study of natural philosophy than by considering the physical phenomena of a *bubble* (originally: *candle*).

There is indeed a large amount of Fluid Mechanics at play in the phenomena ruling the life, death, and descendants of a bubble.

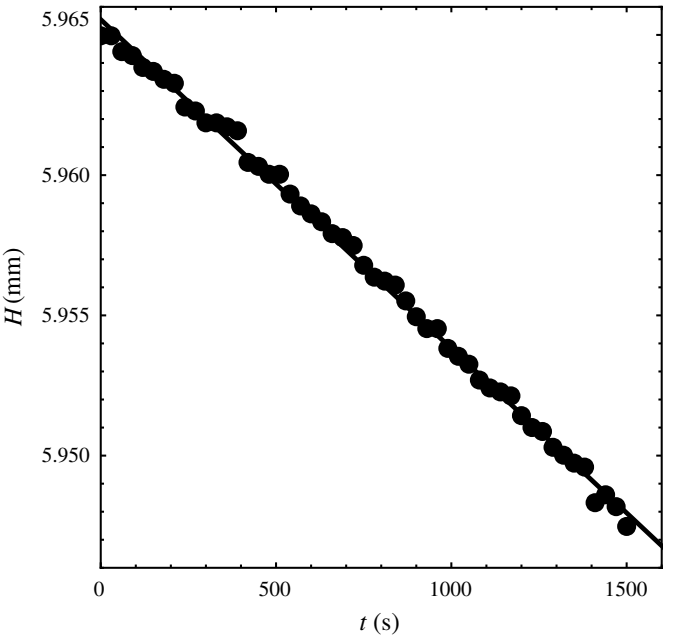

FIGURE 25. Evolution in time of the thickness H of a tapwater layer evaporating in the standard conditions of the laboratory (quiescent air at temperature 20.5 °C, water is thermalized, air hygrometry is 65% of the saturation). The measurement is made by weighting the liquid contained in a circular Petri dish 95 mm in diameter and 12.5 mm deep, with a 1 mg precision balance. The line is the best linear fit giving an evaporation velocity of 11.7 nm s^{-1}.

Acknowledgements

This work has been supported by the Agence Nationale de la Recherche (ANR) through grant ANR-05-BLAN-0222-01.

Appendix A. Bubble geometry

Surface bubbles are shaped by both surface tension and gravity. As justified at the end of § 2.2.1, relative variations in surface tension are small and the cap thickness is rapidly so small that they can be neglected in the following derivation of the bubble shape. Following the same approach as Toba (1959), the bubble interface profile is separated into three portions:

(*a*) the cavity interface up to the cap;

(*b*) the external meniscus from the cap to the surface reference level far away;

(*c*) the cap, both interfaces of which are considered to lie on the same line.

Those three portions meet at the *a priori* unknown point corresponding to $\theta = \theta_c$. A shooting method in which θ_c is set arbitrarily and then progressively adjusted to satisfy a matching condition is therefore required. The set of equations with their matching condition has to be solved for every bubble size prescribed by the parameter R_0/a, where R_0 is the cavity curvature radius at its bottom (in $\theta = \pi$) and a is the yet to be defined capillary length.

Once the parameter R_0/a has been chosen, the profile is built in three successive steps. The cavity profile $\{r, z\}$ (where the origin of heights $z = 0$ is taken at the cavity

bottom, i.e. where $\theta = \pi$) is first obtained by numerically solving

$$\left.\begin{array}{l} \dfrac{\partial(r\sin\theta)}{\partial r} = r\left(\dfrac{2}{R_0} + \dfrac{z}{a^2}\right) \quad \text{for } \theta \in [\theta_c, \pi] \\ \text{with initial condition } \{r, z, \theta\} = \{0, 0, \pi\} \end{array}\right\} \tag{A 1}$$

that equilibrates the cavity pressure with hydrostatic and capillary ones. The profile is integrated from π to the expected value θ_c.

The assumptions of weightless cap and uniform surface tension impose the cap curvatures to be uniform and its profile thus becomes a simple arc of circle. Only one cap is compatible with a given θ_c which has a radius

$$R = \frac{r_c}{\sin\theta_c} \tag{A 2}$$

and $\{0, z_c - R\cos\theta_c\}$ as its centre; where r_c and z_c are the values in θ_c from integration of (A 1). This sets the cavity over-pressure $4\sigma/R$ with respect to the atmosphere (neglecting the air density) and with it the surface of the undisturbed level at infinity

$$\frac{z_\infty}{a^2} = \frac{4\sin\theta_c}{r_c} - \frac{2}{R_0}. \tag{A 3}$$

The external meniscus profile is finally determined by numerically integrating

$$\left.\begin{array}{l} \dfrac{z''}{\left(1+z'^2\right)^{3/2}} + \dfrac{z'}{r\left(1+z'^2\right)^{1/2}} = \dfrac{z - z_\infty}{a^2} \quad \text{for } r \in [r_c, \infty[\\ \text{with the initial condition } \{r, z, z'\} = \{r_c, z_c, \tan\theta_c\}. \end{array}\right\} \tag{A 4}$$

The surface level $z(r \to \infty)$ is compared to the expected value z_∞ it has to match, and depending on the agreement, a new loop with an adjusted value of θ_c is performed or not. Once the desired precision is reached, the latest value of θ_c is used, and the profile is obtained by combination of the three sub-portions as shown in figures 2 and 4.

Appendix B. Bubble cap Poiseuille flow

Consider a curved thin liquid film of viscosity η and density ρ adopting the shape of a cap symmetric with respect to the ascendant vertical direction $\boldsymbol{e_z}$. The film is sandwiched between two mobile layers of a rigid surfactant. We assume that this symmetry extends to the film thickness h whose typical value is small compared with the cap radius R and we therefore seek one-dimensional solutions $h(\theta, t)$ for the film thinning, where θ is the angular coordinate whose origin is at the north pole along $\boldsymbol{e_z}$. For a no-slip condition imposed at the surface by the immobile layers, the viscous flow can be described by the lubrication approximation

$$\boldsymbol{q} = -\frac{(\boldsymbol{\nabla} p + \boldsymbol{f})\, h^3}{12\,\eta}, \qquad \frac{\partial h}{\partial t} = -\boldsymbol{\nabla}\boldsymbol{q} \tag{B 1}$$

where $\boldsymbol{q}$ is the flow per unit length through a normal section of the film, the pressure gradient $\boldsymbol{\nabla} p$ is zero all over the cap and the external tangential force $\boldsymbol{f}\cdot\boldsymbol{e_\theta}$ acting on the film reduces here to the gravity body force $-\rho g h\,\boldsymbol{e_z}\cdot\boldsymbol{e_\theta} = -\rho g h\sin(\theta)$. Non-dimensionalizing length by a typical initial thickness h_0 and times by $12\eta R/\rho g h_0^2$, one obtains

$$\frac{\partial h}{\partial t} = -\frac{1}{\sin\theta}\frac{\partial(h^3\sin^2\theta)}{\partial\theta}. \tag{B 2}$$

Seeking solutions of the form $h(\theta, t) = F(\theta) \times G(t)$ yields

$$\frac{\dot{G}}{G^3} = -\frac{(F^3 \sin^2\theta)'}{F \sin\theta} = \mathscr{A} \tag{B 3}$$

where the prime and overdot stand for derivation with respect to θ and t, respectively, and $\mathscr{A}$ is a constant. Integration of (B 3) gives

$$F(\theta) = \frac{\left(-\dfrac{2\mathscr{A}}{3}\displaystyle\int_0^\theta \sin^{1/3}\theta \, \mathrm{d}\theta\right)^{1/2}}{\sin^{2/3}\theta}. \tag{B 4}$$

With the initial condition $h(0, 0) = h_0$ and considering $F(0) = G(0) = 1$, one has $\mathscr{A} = -2$ and therefore

$$G(t) = (1 + 4\,t)^{-1/2}. \tag{B 5}$$

Finally, the film thickness $h(\theta, t)$ is written in dimensional variables

$$h(\theta, t) = \frac{\left(4/3\displaystyle\int_0^\theta \sin^{1/3}\theta \, \mathrm{d}\theta\right)^{1/2}}{\sin^{2/3}\theta} \frac{1}{\left(\dfrac{1}{h_0^2} + \dfrac{\rho g t}{3\eta R}\right)^{1/2}}. \tag{B 6}$$

This thinning law, which amounts to $h \sim \sqrt{4\eta R/\rho g\, t}$ once the initial condition h_0 has been forgotten, i.e. after a characteristic time $\eta R/\rho g h_0^2$, does not depend on the cap extension θ_c (see figure 2). It is prescribed by the conditions at the pole and thus solely depends on the radius of curvature R. The function $F(\theta)$ is plotted in figure 26 where it is seen to be almost uniform over the whole cap. Its maximum value at the cap equator is only $2\,\pi^{1/4}\sqrt{\Gamma(2/3)/\,\Gamma(7/6)} \simeq 1.31$ times that at the pole.

Note that solution (B 6) has been derived and used by Couder *et al.* (2005) to describe the air film upward drainage of a surface anti-bubble whose shape is that of an upside-down classical surface bubble.

Appendix C. Turbulence features

As mentioned in § 3.2, a global translation of the film, whose intensity is measured by $\sqrt{\langle \boldsymbol{u}^2 \rangle}$, is not likely to induce thickness modulations leading to film rupture. On the contrary, localized stretching, if it is intense enough at the scale of the film thickness h itself, will. This condition is, however, much more restrictive. We measured velocity increments $\delta\boldsymbol{u} = \boldsymbol{u}(\boldsymbol{r}) - \boldsymbol{u}(\boldsymbol{r} + \delta\boldsymbol{r})$ for various increment sizes in the horizontal, and vertical directions $\delta\boldsymbol{r} = (\delta x, \delta z)$ using the velocity fields studied in § 3.2. Distribution functions of the horizontal velocity component increments in the horizontal direction $\delta u = u(x) - u(x + \delta x)$ and their second moment $\langle \delta u^2 \rangle$ are plotted in figure 27 for various values of δx.

For two-dimensional turbulence, where enstrophy $\langle (\boldsymbol{\nabla} \times \boldsymbol{u})^2 \rangle$ is, together with kinetic energy $\langle \boldsymbol{u}^2 \rangle$, a conserved quantity in the inertial range, one expects that the flow for scales smaller than the injection scale is represented by the enstrophy direct cascade (Kraichnan 1967); it has been observed in soap films (Kellay, Wu & Goldburg 1995). For a stationary enstrophy injection rate β, the energy spectrum for wavenumber k is thus $E(k) \sim \beta^{2/3} k^{-3}$ or equivalently

$$\langle \delta\boldsymbol{u}^2 \rangle \sim \beta^{2/3} \delta\boldsymbol{r}^2 \tag{C 1}$$

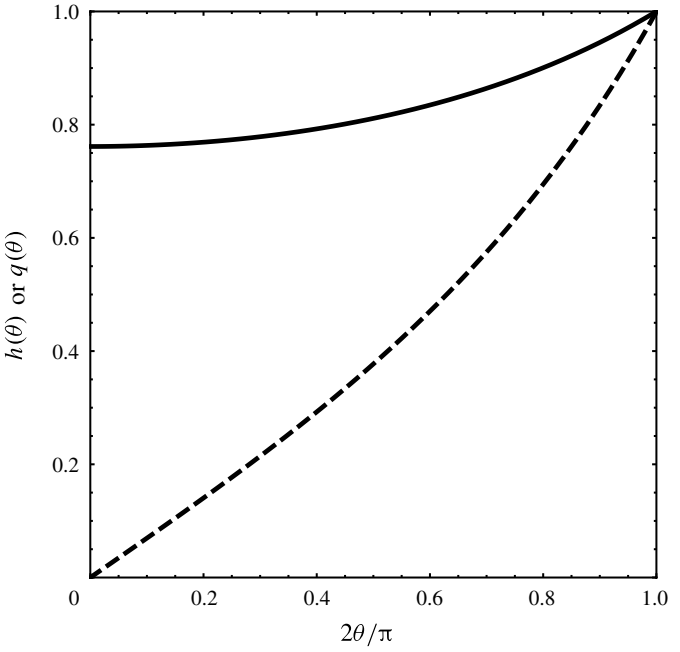

FIGURE 26. Thickness $h \propto F(\theta)$ (—) and flow rate $q \propto F(\theta)^3 \sin\theta$ (−−) dependence on the angular coordinate θ at any time t. Values are divided by the corresponding values at the equator, at $\theta = \pi/2$.

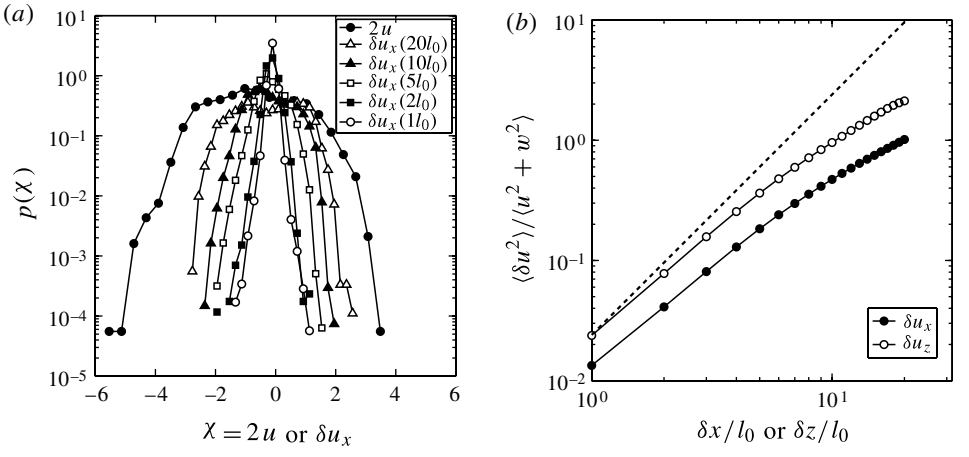

FIGURE 27. (*a*) Probability distribution function of horizontal velocities $u = \boldsymbol{u} \cdot \boldsymbol{e_x}$ and of horizontal–horizontal velocity increments $\delta u_x(\delta x) = u(x) - u(x + \delta x)$ accumulated over 100 velocity fields. Increment distances are $\delta x = 1, 2, 5, 10$ and $20l_0$, where $l_0 = 225$ μm is the field spatial resolution (half that appearing on figure 14). (*b*) Second moments of velocity increment distributions $\langle \delta u_x^2 \rangle$ and $\langle \delta u_z^2 \rangle$. The dashed line is the law $\langle \delta u^2 \rangle \propto \delta \boldsymbol{r}^2$ of (C 1).

like for a passive scalar in a direct smooth cascade (the thickness field in a soap film has also been suggested to follow Batchelor scaling (Amarouchene & Kellay 2004)).

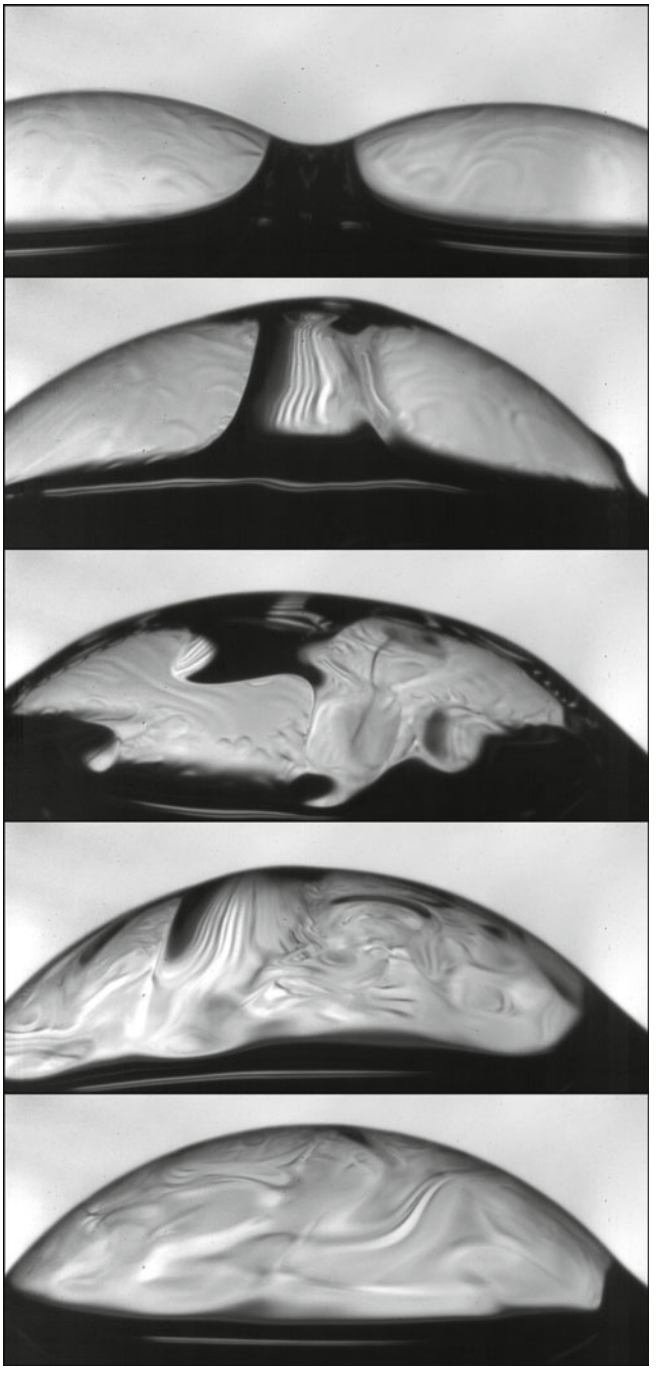

FIGURE 28. Evolution of two bubbles with radii $R = 5.6$ mm coalescing. Comparatively to the volume of both caps, a large volume of water is contained in the meniscus border initially joining them. As coalescence initiates, this volume is pushed up into the newly formed cap and is rapidly spread over it by convection. This results in a new bubble which has no memory of the history of the two separated bubbles that have merged. A time interval of 17, 50, 117 and 250 ms has respectively elapsed from the top image to the bottom.

In figure 27, the velocity increments are roughly following a square δx^2 law (although the best fit is shallower, suggesting that the displayed range of scales is not far from the inverse energy cascade range). The corresponding enstrophy transfer rate is $\beta \sim 10^5$ s^{-3} and the associated dissipation scale

$$r \sim (\nu^2/\beta^{2/3})^{1/4} \sim 100\ \mu\text{m}. \tag{C 2}$$

This scale is somewhat larger than the film thickness h, but even at that overestimated scale, $\langle \delta u\,(r)^2 \rangle$ is found to be of order

$$\langle \delta u\,(r)^2 \rangle \sim \beta^{2/3} r^2 \sim 10^{-5}\ \text{m}^2\ \text{s}^{-2}, \tag{C 3}$$

very far away in order of magnitude from the square of the typical Culick film opening velocity

$$V^2 = 2\sigma/\rho h \sim 1\text{–}10\ \text{m}^2\ \text{s}^{-2} \tag{C 4}$$

that sets the velocity fluctuation threshold to overcome stabilization by surface tension. This is consistent with the observation in figure 15 that the film opens immediately after a hole nucleation event on a basically stationary velocity field (and associated thickness field).

In conclusion, turbulent motions induced by marginal regeneration alone are definitely too weak to provoke film rupture.

Appendix D. Coalescence

This appendix shows, by way of figure 28, how the coalescence of two nearby bubbles at the pool surface resets their individual drainage past history. Indeed, one sees that a large fraction of liquid in the menisci at the foot of the bubbles is re-injected into the coalesced bubble cap, hence producing a 'young' bubble, irrespective of the age of the initial separated bubbles. This legitimates the assumption made in § 5.2 that the evolution of an isolated bubble is relevant for describing the spray structure, including for an assembly of interacting bubbles.

REFERENCES

AITKEN, J. 1881 Dust, fog, and clouds. *Nature* **23**, 384–385.

AMAROUCHENE, Y. & KELLAY, H. 2004 Batchelor scaling in fast-flowing soap films. *Phys. Rev. Lett.* **93** (21), 214504.

ANDREAS, E. L., EDSON, J. B., MONAHAN, E. C., ROUAULT, M. P. & SMITH, S. D. 1995 The spray contribution to net evaporation from the sea: a review of recent progress. *Boundary-Layer Meteorol.* **72**, 3–52.

ARADIAN, A., RAPHAËL, E. & DE GENNES, P. G. 2001 Marginal pinching in soap films. *Europhys. Lett.* **55** (6), 834–840.

BARGER, W. R., DANIEL, W. H. & GARRETT, W. D. 1974 Surface chemical properties of banded sea slicks. *Deep-Sea Res.* (I) **21**, 83–89.

BIRD, J. C., DE RUITER, R., COURBIN, L. & STONE, H. A. 2010 Daughter bubble cascade produced by folding of ruptured thin films. *Nature* **465**, 759–762.

BLANCHARD, D. 1963 The electrification of the atmosphere by particles from bubbles in the sea. PhD thesis, Woods Hole Oceanographic Institution.

BLANCHARD, D. C., BILOFSKY, H. S. & BRIDGMAN, W. B. 1972 The effervescence of ocean surf. *J. Chem. Educ.* **49** (1), 29–30.

BLANCHARD, D. C. & SYSDEK, L. D. 1988 Film drop production as a function of bubble size. *J. Geophys. Res.* **93** (C4), 3649–3654.

BOUCHIAT, M. & MEUNIER, J. 1971 Spectre des fluctuations thermiques de la surface libre d'un liquide simple. *J. Phys.* **32**, 561–571.

BREWARD, C. J. & HOWELL, P. D. 2002 The drainage of a foam lamella. *J. Fluid Mech.* **458**, 379–406.

BRUINSMA, R. 1995 Theory of hydrodynamic convection in soap films. *Physica* A **213**, 59–76.

BULL, L. 1904 Rupture d'un film de savon par un projectile. Environ 1500 images/seconde. Stereoscopic Movie – Institut E.-J. Marey.

CASTELETTO, V., CANTAT, I., SARKER, D., BAUSCH, R., BONN, D. & MEUNIER, J. 2003 Stability of soap films: hysteresis and nucleation of black films. *Phys. Rev. Lett.* **90** (4).

COANTIC, M. 1980 Mass transfert across the ocean–air interface: small scale hydrodynamic and aerodynamic mechanisms. *Physico-Chem. Hydrodyn.* **1**, 249–279.

COUDER, Y., FORT, E., GAUTIER, C. H. & BOUDAOUD, A. 2005 From bouncing to floating: noncoalescence of drops on a fluid bath. *Phys. Rev. Lett.* **94** (4), 177801.

CULICK, F. E. C. 1960 Comments on a ruptured soap film. *J. Appl. Phys.* **31**, 1128.

DEANE, G. B. & STOKES, D. 2002 Scale dependence of bubble creation mechanisms in breaking waves. *Nature* **418**, 839–844.

DEBRÉGEAS, G., DE GENNES, P. G. & BROCHARD-WYART, F. 1998 The life and death of 'bare' viscous bubbles. *Science* **279**, 1704–1707.

DUPRÉ, A. 1869 *Théorie Mécanique de la Chaleur*. Gauthiers-Villars.

EGGERS, J. & VILLERMAUX, E. 2008 Physics of liquid jets. *Rep. Prog. Phys.* **71**, 36601.

FARADAY, M. 1861 *A Course of Six Lectures on the Chemical History of a Candle*. Royal Society (Copyright 1988 Chicago Review Press).

DE GENNES, P. G. 2001 Young soap films. *Langmuir* **17**, 2416–2419.

HAGEN, G. 1846 Über die oberfläche der flüssigkeiten. *Ann. Poggendorff* **67** (1), 152.

HOWELL, P. D. 1999 The draining of a two dimensional bubble. *J. Engng Maths* **35**, 251–272.

JACOBS, W. C. 1937 Preliminary reports on the study of atmospheric chlorides. *Mon. Weath. Rev.* **65**, 147–151.

JARVIS, N. L., GARRETT, W. D., SCHEIMAN, M. A. & TIMMONS, C. O. 1967 Surface chemical characterization of surface-active material in seawater. *Limnol. Oceanogr.* **12**, 88–96.

KELLAY, H., WU, X. L. & GOLDBURG, W. I. 1995 Experiments with turbulent soap films. *Phys. Rev. Lett.* **74** (20), 3975 4.

KNELMAN, F. H., DOMBROWSKI, N. & NEWITT, D. M. 1954 Mechanism of the bursting of bubbles. *Nature* **173**, 261.

KRAICHNAN, R. 1967 Inertial ranges in two-dimensional turbulence. *Phys. Fluids* **10**, 1417–1423.

LATHAM, J. & SMITH, M. H. 1990 Effect on global warming of wind-dependent aerosol generation at the ocean surface. *Nature* **347**, 372–373.

LHUISSIER, H. & VILLERMAUX, E. 2009 Bursting bubbles. *Phys. Fluids* **21**, 091111.

LIDE, D. R. (Ed.) 1999 *Handbook of Chemistry and Physics*, 79th edn CRC.

MARANGONI, C. & STEFANELLI, P. 1872 Monografia sulle bolle liquide. *Nuovo Cimento* **7-8** (1), 301–356.

MARIS, H. J. 2006 Introduction to the physics of nucleation. *C. R. Phys.* **7**, 946–958.

MEUNIER, P. & LEWEKE, T. 2003 Analysis and minimization of errors due to high gradients in particle image velocimetry. *Exp. Fluids* **35**, 408–421.

MONAHAN, E. C. & DAM, H. G. 2001 Bubbles: an estimate of their role in the global oceanic flux. *J. Geophys. Res.* **106**, 9377–9383.

MYSELS, K. J., SHINODA, K. & FRANKEL, S. 1959 *Soap Films, Studies of their Thinning and a Bibliography*. Pergamon.

NEWITT, D. M., DOMBROWSKI, N. & KNELMAN, F. H. 1954 Liquid entrainment. 1. The mechanism of drop formation from gas or vapour bubbles. *Trans. Inst. Chem. Engrs* **32**, 244–261.

NIERSTRASZ, V. A. & FRENS, G. 1998 Marginal regeneration in thin vertical liquid films. *J. Colloid Interface Sci.* **207**, 209–217.

O'DOWD, C. & DE LEEUW, G. 2007 Marine aerosol production: a review of the current knowledge. *Phil. Trans. R. Soc. Lond.* A **365**, 1753–1774.

PLATEAU, J. 1873 *Satique expérimentale et théorique des liquides soumis aux seules forces moléculaires*. Ghauthier-Villard.

PREOBRAZHENSKII, L. 1973 Estimate of the content of spray-drops in the near-water layer of the atmosphere. *Fluid Mech. -Sov. Res.* **2**, 95–100.

RESCH, F. & AFETI, G. 1991 Film drop distribution from bubbles bursting in seawater. *J. Geophys. Res.* **96** (C6), 10681–10688.

SCHWARTZ, L. W. & ROY, R. V. 1999 Modelling draining flow in mobile and immobile soap films. *J. Colloid Interface Sci.* **218**, 309–323.

SPIEL, D. E. 1998 On the birth of film drops from bubbles bursting on seawater surfaces. *J. Geophys. Res.* **103** (C11), 24907–24918.

TAYLOR, G. I. 1959 The dynamics of thin sheets of fluid III. desintegration of fluid sheets. *Proc. R. Soc. Lond.* A **253**, 313–321.

TOBA, Y. 1959 Drop production by bursting of air bubbles on the sea surface. ii theoretical study on the shape of floating bubbles. *J. Oceanogr. Soc. Japan* **15**, 121–130.

VAN KAMPEN, N. G. 1981 *Stochastic Processes in Chemistry and Physics*. North-Holland.

VILLERMAUX, E. 2007 Fragmentation. *Annu. Rev. Fluid Mech.* **39**, 419–446.

VILLERMAUX, E., MARMOTTANT, P. & DUPLAT, J. 2004 Ligament-mediated spray formation. *Phys. Rev. Lett.* **92** (7).

WORTHINGTON, A. M. & COLE, R. S. 1897 Impact with a liquid surface, studied by the aid of instantaneaous photography. *Phil. Trans. R. Soc. Lond.* A **189**, 149–166.

WU, J., MURRAY, J. & LAI, R. 1984 Production and distributions of sea spray. *J. Geophys. Res.* **89** (C5), 8163–8169.

XIA, H., SHATS, M. & FALKOVICH, G. 2009 Spectrally condensed turbulence in thin layers. *Phys. Fluids* **21**, 125101.

ZHENG, Q. A., KLEMAS, V. & HSU, Y.-H. L. 1983 Laboratory measurements of water surface bubble life time. *J. Geophys. Res.* **88**, 701–706.